Application of The Moment Method in The Spectral Domain

Mamdoh Gharbi, Adnan Affandi, Sami Ali

Department of Electrical and Computer Engineering, King Abdul Aziz University, P O Box:80204, Jeddah 21589
mamdohgharbi@yahoo.com

Abstract: The Moment Method (MM) is employed in the spectral domain where piece-wise sinusoidal basis functions are used to expand the current distribution on the dipole. The current distribution and input impedance are calculated as functions of the layers parameters. The effects of the material anisotropy and superstrate (cover) parameters are studied. Expressions for the far-zone fields of the dipole in the anisotropic substrate-superstrate structure are derived, and radiation patterns are computed for different structure parameter. Finally, Improvement of Single-Element Antenna Design by using anisotropic layer will be demonstraited.
[Affandi A, Gharbi M, Ali S. **Application of The Moment Method Spectral Integral Domain.** *Life Sci J* 2015;12(5):1-23]. (ISSN:1097-8135). http://www.lifesciencesite.com. 1

Keywords: Moment method; dyadic Green's function; current distribution; input impedance

1. Introduction

Extensive amount of work is being carried out in the analysis of various parameters associated with antennas on anisotropic substrates (Deschamps, 1953) (Gutton and Baissinot, 1955). Study has also been carried out using hertz vector potentials (Carver and Mink, 1981). A full wave analysis for antenna on a double dielectric anisotropic substrate has also been done (Byron, 1970). A recent study includes anisotropic substrate characterized by permittivity and permeability tensors (Munson, 1974).

In our study the mixed boundary value problem of a microstrip dipole placed on the top of a uniaxially anisotropic substrate with the presence of a superstrate (cover) layer as shown in Figure. 2.1. The cover layer can be either isotropic or uniaxially anisotropic dielectric. The microstrip dipole is assumed to be excited by an idealized source. This idealized source provides the incident electric field, which excites current on the dipole surface. Explicit form of the spectral domain electric field integral equation (EFIE) for the surface current induced on the dipole is derived using the dyadic Green's function for the layered uniaxially anisotropic medium. The EFIE is solved using the MM to find the unknown induced surface current on the microstrip dipole. Piecewise sinusoidal (PWS) expansion modes are used to represent the unknown surface current. Explicit expressions for the input impedance are obtained for different electrical and geometrical parameters. Antenna research was conducted to explore various methods of designing an antenna that operates both effectively and efficiently within the previously mentioned design constraints. After performing extensive research, the Yagi-Uda array and Microstrip Patch antenna array were deemed to be topologies that could effectively operate within the design constraints. Multiple designs, simulations, and analyses were conducted to provide insight on the advantages and disadvantages of both topographies. Ultimately the Microstrip Patch array was chosen due to its ease of impedance-matching with a 50-Ω SMA line input. The ideal outcome of the design is to produce a highly directive antenna. As such, it is necessary to implement an array of patch antenna elements to promote greater directivity and gain. 1-element antennas were designed, simulated, and analyzed. For simplicity and ease of mathematical calculations, patch antenna elements were separated by a constant distance of λ/2.

2. Spectral Domain Integral Equation

The microstrip dipole considered in Figure 2.1 is of length *L* and width *W*.

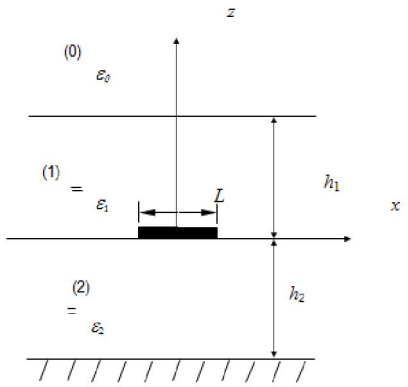

Figure 2.1. Geometry of the Problem

It is assumed that the width of the dipole is very small compared to the free-space wavelength ($W <<$ $_o$), and therefore the current on the dipole can be assumed to have only one component in the *x*-direction. That is $\overline{J}_s = \hat{x}\, J_s$.

The dielectric layers are characterized by permittivity and permeability tensors of the form

$$\overline{\overline{\varepsilon}}_j = \begin{bmatrix} \varepsilon_j & 0 & 0 \\ 0 & \varepsilon_j & 0 \\ 0 & 0 & \varepsilon_{jz} \end{bmatrix} \tag{2.1}$$

and

$$\overline{\overline{\mu}}_j = \mu_0 \overline{\overline{I}}$$

where $\overline{\overline{I}}$ is the unit dyadic.

The electric field integral equation EFIE on the surface S of the microstrip dipole can be written as:

$$-\overline{E}_t^{(s)} = \overline{E}_t^{(i)} \quad ,$$

where(t) stands for tangential components to the surface of the printed dipole and

$$\overline{E}_t^{(s)}(\bar{r}) = i\omega \iint_S d\bar{r}' \, \overline{\overline{G}}_{11}^{T}(\bar{r},\bar{r}') \cdot \bar{J}_s(\bar{r}') \tag{2.2}$$

where $\overline{\overline{G}}_{11}^{T}(\bar{r},\bar{r}')$ is the transverse 2x2 dyadic Green's function which is written as below with k_{jz} replaced by $k_{1z}^{(h)}$ for TE waves and k_{jz} replaced by $k_{1z}^{(e)}$ for TM waves, we get:

$$\overline{\overline{G}}_{11}(\bar{r},\bar{r}')\Big|_{z'=0} = \int_{-\infty}^{\infty}\int d\bar{k}_s \, e^{\bar{k}_s\cdot(\bar{r}_s-\bar{r}_s')} \, \overline{\overline{g}}_{11}(\bar{k}_s,z)$$

$$\overline{\overline{g}}_{11}(\bar{k}_s,z) = \frac{i\mu_0}{8\pi^2}\left\{\frac{r_1^{TE}}{k_{1z}^{(h)}}\left[\hat{h}(k_{1z}^{(h)})e^{ik_{1z}^{(h)}z} + R_{\cup 1}^{TE}e^{2ik_{1z}^{(h)}h_1}\hat{h}(-k_{1z}^{(h)})e^{-ik_{1z}^{(h)}z}\right]\right.$$
$$\left.\left[\hat{h}(k_{1z}^{(h)}) + R_{\cap 1}^{TE}\hat{h}(-k_{1z}^{(h)})\right]\right.$$
$$+\frac{r_1^{TM}}{k_{1z}^{(e)}}\left[\hat{v}(k_{1z}^{(e)})e^{ik_{1z}^{(e)}z} + R_{\cup 1}^{TM}e^{2ik_{1z}^{(e)}h_1}\hat{v}(-k_{1z}^{(e)})e^{-ik_{1z}^{(e)}z}\right]$$
$$\left[\hat{v}(k_{1z}^{(e)}) + R_{\cap 1}^{TM}\hat{v}(-k_{1z}^{(e)})\right] \tag{2.3}$$

where

$$R_{\cup 1}^{TE} = R_{10}^{TE} = \frac{k_{1z}^{(h)} - k_{0z}}{k_{1z}^{(h)} + k_{0z}} \tag{2.4}$$

$$R_{\cap 1}^{TE} = \frac{k_{2z}^{(h)} + ik_{1z}^{(h)} \tan k_{2z}^{(h)}h_2}{-k_{2z}^{(h)} + ik_{1z}^{(h)} \tan k_{2z}^{(h)}h_2} \tag{2.5}$$

$$R_{\cup 1}^{TM} = R_{10}^{TM} = \frac{k_{1z}^{(e)} - \varepsilon_1 k_{0z}}{k_{1z}^{(e)} + \varepsilon_1 k_{0z}} \tag{2.6}$$

$$R_{\cap 1}^{TM} = \frac{\varepsilon_2 k_{1z}^{(e)} + i\varepsilon_1 k_{2z}^{(e)} \tan k_{2z}^{(e)}h_2}{\varepsilon_2 k_{1z}^{(e)} - i\varepsilon_1 k_{2z}^{(e)} \tan k_{2z}^{(e)}h_2} \tag{2.7}$$

$$r_1^{TE} = \frac{1}{1 - R_{\cap 1}^{TE} R_{\cup 1}^{TE} e^{2ik_{1z}^{(h)}h_1}} \tag{2.8}$$

$$r_1^{TM} = \frac{1}{1 - R_{\cap 1}^{TM} R_{\cup 1}^{TM} e^{2ik_{1z}^{(e)}h_1}} \tag{2.9}$$

$$k_{jz}^{(h)} = \left(k_j^2 - k_s^2\right)^{1/2} \tag{2.10}$$

$$k_{jz}^{(e)} = \left(k_j^2 - \frac{\varepsilon_j}{\varepsilon_{jz}} k_s^2\right)^{1/2} \tag{2.11}$$

$$k_j^2 = \omega^2 \mu_0 \varepsilon_j \tag{2.12}$$

$$k_{0z} = \left(k_0^2 - k_s^2\right)^{1/2} \tag{2.13}$$

$$k_0^2 = \omega^2 \mu_0 \varepsilon_0 \tag{2.14}$$

where $j = 1,2$.

The sommerfeld condition at infinity determines the branch interpretation of

$k_{0z} = \left(k_0^2 - k_s^2\right)^{1/2}$ as:

$k_{0z} = \left|\left(k_0^2 - k_s^2\right)^{1/2}\right|$, $\quad |k_s| \le k_0$

$\mathrm{Re}(k_{0z}) \ge 0$, and

$k_{0z} = i\left|\left(k_s^2 - k_0^2\right)\right|$, $\quad |k_s| \ge k_0$

i.e $\mathrm{Im}(k_{0z}) \ge 0$.

In the above $\mathrm{Re}(k_{0z})$ and $\mathrm{Im}(k_{0z})$ stand for real and imaginary parts respectively.

That is the positive branch of the square root has been properly chosen to be consistent with the radiation condition as $z \to \infty$.

The unit vectors $\hat{h}(k_{jz})$ and $\hat{v}(k_{jz})$ are obtained as

$$\hat{h}(k_{jz}^{(h)}) = \hat{h}(-k_{jz}^{(h)}) = \frac{1}{k_s}(\hat{x}k_y - \hat{y}k_x) = \hat{h} \tag{2.15}$$

$$\hat{v}(\pm k_{jz}^{(e)}) = \mp\frac{k_{jz}^{(e)}}{k_j k_s}(\hat{x}k_x + \hat{y}k_y) + \hat{z}\frac{\varepsilon_j}{\varepsilon_{jz}}\frac{k_s}{k_j} = \mp\hat{u}(k_{jz}^{(e)}) + \hat{z}\frac{\varepsilon_j}{\varepsilon_{jz}}\frac{k_s}{k_j} \tag{2.16}$$

where $j = 1, 2$.

The expression for the transverse (surface) components of $\overline{\overline{g}}_{11}(\bar{k}_s, z=0)$

Is

$$\bar{\bar{g}}_{11}^{T}(\bar{k}_s, z=0) = \frac{i\mu_0}{8\pi^2}\left\{\frac{r_1^{TE}}{k_{1z}^{(h)}}\left(1+R_{\cup 1}^{TE}e^{2ik_{1z}^{(h)}h_1}\right)\left(1+R_{\cap 1}^{TE}\right)\hat{h}\hat{h} + \frac{r_1^{TM}}{k_{1z}^{(e)}}\left(1-R_{\cup 1}^{TM}e^{2ik_{1z}^{(e)}h_1}\right)\left(1-R_{\cap 1}^{TM}\right)\hat{u}(k_{1z}^{(e)})\hat{u}(k_{1z}^{(e)})\right\} \quad (2.17)$$

Since the induced surface current density on the dipole is assumed to be in the *x*-direction, only the (x,x) component of $\bar{\bar{G}}_{11}$ will be required. Thus,

$$\bar{\bar{g}}_{11}^{(x,x)}(\bar{k}_s) = \frac{i\mu_0}{8\pi^2}\left\{\frac{k_y^2}{k_s^2}\cdot\frac{r_1^{TE}}{k_{1z}^{(h)}}\left(1+R_{\cup 1}^{TE}\,e^{2ik_{1z}^{(h)}h_1}\right)\left(1+R_{\cap 1}^{TE}\right) + \frac{k_x^2}{k_s^2}\frac{k_{1z}^{(e)}}{k_1^2}r_1^{TM}\left(1-R_{\cup 1}^{TM}e^{2ik_{1z}^{(e)}h_1}\right)\left(1-R_{\cap 1}^{TM}\right)\right\}\hat{x}\,\hat{x} \quad (2.18)$$

Substituting Eq. 2.3 in Eq. 2.2 with $z = 0$,

$$\bar{E}_t^{(s)}(\bar{r}_s) = i\omega\iint_S d\bar{r}_s'\int_{-\infty}^{\infty}\int d\bar{k}_s\, e^{i\bar{k}_s\cdot\bar{r}_s}\,\bar{\bar{g}}_{11}^{(x,x)}(\bar{k}_s)\cdot e^{-i\bar{k}_s\cdot\bar{r}_s'}\,\bar{J}_s(\bar{r}_s') \quad (2.19)$$

Using the 2-D Fourier Transform, Eq 2.19 reduces to:

$$\bar{E}_t^{(s)}(\bar{r}_s) = i\omega\int_{-\infty}^{\infty}\int d\bar{k}_s\, e^{i\bar{k}_s\cdot\bar{r}_s}\,\bar{\bar{g}}_{11}^{(x,x)}(\bar{k}_s)\cdot\bar{J}_s(\bar{k}_s) \quad (2.20)$$

where $\bar{J}_s(\bar{k}_s)$ is the Fourier Transform of the surface current density $\bar{J}_s(\bar{r}_s)$ .using electric field integral equation (EFIE) for the unknown surface current density $\bar{J}_s$

and $-\bar{E}_t^{(s)} = \bar{E}_t^{(i)}$,

getting

$$-i\omega\int_{-\infty}^{\infty}\int d\bar{k}_s e^{i\bar{k}_s\cdot\bar{r}_s}\;\bar{\bar{g}}_{11}^{(x,x)}(\bar{k}_s)\cdot\bar{J}_s(\bar{k}_s) = \bar{E}^{(i)}(\bar{r}_s),\quad \bar{r}_s\in S \quad (2.21a)$$

$$\int_{-\infty}^{\infty}\int d\bar{k}_s e^{i\bar{k}_s\cdot\bar{r}_s}\;\bar{J}_s(\bar{k}_s) = 0,\quad \bar{r}_s\notin S \quad (2.21b)$$

Eqs. 2.21 are the coupled set vector integral equations in the spectral domain. Eq. 2.21a is the spectral domain electric field integral equation (SDEFEI).

2.1. Application of the Moment Method (MM)Solution

To apply the MM to solve Eq. 2.21, the surface current density on the dipole is expanded in terms of appropriate expansion modes $\bar{f}_n(x,y)$ with unknown coefficients I_n:

$$\bar{J}_s(\bar{r}_s') = \hat{x}\sum_{n=1}^{N} I_n\, f_n(x',y') \quad \text{(A/m)} \quad (2.22)$$

where

$$f_n(x',y') = \Phi_n(x')\,\Psi_n(y') \quad (2.23)$$

For the present work, Piecewise sinusoidal (PWS) expansion modes are selected to represent the variation of the current in the x-direction.

The form of the n^{th} expansion function centered about x_n may be expressed mathematically as:

$$\Phi(x') = \begin{cases}\dfrac{\sin k(x'-x_{n-1})}{\sin kd}, & x_{n-1}\le x' < x_n \\ \dfrac{\sin k(x_{n+1}-x')}{\sin kd}, & x_n \le x' < x_{n+1} \\ 0, & \text{otherwise}\end{cases} \quad (2.24)$$

where $x_n = nd$, and d is the half length of each expansion mode given by $d = L/N$.

The wavenumber k for the PWS mode can be chosen arbitrary, however, a judicious choice will improve the convergence. For single isotropic substrate, it was found that setting k equal to the "effective" wave number for the substrate is a good choice (Pozar, 1983)

$$k = k_e = \sqrt{\varepsilon_e}\;k_0 \quad (2.25)$$

The *y*-variation of the current density may be chosen as

$$\Psi_n(y') = \frac{1}{W}\quad,\qquad -\frac{W}{2} < y' < \frac{W}{2} \quad (2.26)$$

Thus, The Fourier transform of the current density $\bar{J}_s(x',y')$ in Eq. 2.26 can be obtained as

$$\bar{J}_s(\bar{k}_s) = \hat{x}\sum_{n=1}^{N} I_n\,\tilde{F}_n(\bar{k}_s) \quad (2.27)$$

where

$$\tilde{F}_n(\bar{k}_s) = \tilde{\Phi}_n(k_x)\,\tilde{\Psi}_n(k_y) \quad (2.28)$$

and

$$\tilde{\Phi}_n(k_x) = \frac{2k_e(\cos k_e d - \cos k_x d)}{\sin k_e d\,(k_x^2 - k_e^2)}\,e^{-ik_x nd} \quad (2.29)$$

$$\tilde{\Psi}_n(k_y) = \frac{\sin k_y\frac{W}{2}}{k_y\frac{W}{2}} \quad (2.30)$$

Substituting Eq. 2.27 in Eq. 2.21, we get

$$-\sum_{n=1}^{N} I_n \, \bar{E}_n^{(s)}(\bar{r}_s) = \bar{E}^{(i)}(\bar{r}_s), \quad on\ S \tag{2.31}$$

where $\bar{E}_n(\bar{r}_s)$ is the scattered electric field due to the n^{th} expansion mode $\bar{f}_n$ of the surface current density $\bar{J}_s$, and is given by

$$\bar{E}_n^{(s)}(\bar{r}_s) = \hat{x} i\omega \int_{-\infty}^{\infty}\int d\bar{k}_s \, e^{i\bar{k}_s\cdot\bar{r}_s} \, g_{11}^{(x,x)}(\bar{k}_s)\, \tilde{F}_n(\bar{k}_s)$$

$$n = 1,2,..,m,...,N \tag{2.32}$$

where $\bar{\bar{g}}_{11}^{(x,x)}(\bar{k}_s)$ is given by Eq. 2.8. Applying the Galerkin's method by choosing the test function to be the same as the expansion functions; dot multiplying Eq. 2.27 by $\bar{f}_m(x,y)$ and integrating over the surface of the dipole, we get

$$-\sum_{n=1}^{N} I_n \iint_{S_m} \bar{f}_m(x,y)\cdot\bar{E}_n^{(s)}(x,y)\,dx\,dy = \iint_{S_m} \bar{f}_m(x,y)\cdot\bar{E}^{(i)}(x,y)\,dx\,dy, \quad m = 1, 2,.., N \tag{2.33}$$

where S_m is the surface of the m^{th} test mode and $\bar{E}_m^{(s)}(x,y)$ is the scattered field in layer (1) by the m^{th} test mode $\bar{f}_m$ at the position of the n^{th} expansion mode.

For the case of impressed current source (probe excitation), by using the reciprocity theorem, Eq. 2.33 can be written as

$$-\sum_{n=1}^{N} I_n \iint_{S_n} \bar{E}_m^{(s)}(x,y)\cdot\bar{f}_n(x,y)\,dx\,dy = \iiint_{V} \bar{E}_m^{(s)}(x,y,z)\cdot\bar{J}^{(i)}(x,y,z)\cdot\,dx\,dy\,dz, \quad m = 1, 2,.., N \tag{2.34}$$

where, $\bar{E}_m^{(s)}(x,y,z)$ is the field in layer(2) of the test mode at the position of the probe and $\bar{J}^{(i)}$ is the impressed (source) current of the probe.

Thus, Eq. 2.33 or Eq. 2.34 can be written as:

$$\sum_{n=1}^{N} Z_{mn} I_n = V_m^P, \quad m = 1, 2,...., N \tag{2.35}$$

where

$$Z_{mn} = -\iint_{S_n} \bar{E}_m^{(s)}(x,y)\cdot\bar{f}_n(x,y)\,dx\,dy \tag{2.36}$$

$$V_m^P = \iiint_{V} \bar{f}_m(x,y)\cdot\bar{E}^{(i)}(x,y)\,dV \tag{2.37a}$$

or

$$V_m^P = \iiint_{V} \bar{E}_m^{(s)}(x,y,z)\cdot\bar{J}^{(i)}(x,y,z)\,dx\,dy\,dz \tag{2.37b}$$

Substituting Eq. 2.32 with $n = m$ in Eq. 2.36 and performing the integration over S_n, we get:

$$Z_{mn} = -i\omega \int_{-\infty}^{\infty}\int dk_x dk_y \, \tilde{F}_m^*(k_x,k_y)\, g_{11}^{(x,x)}(k_x,k_y)\, \tilde{F}_n(k_x,k_y),$$

$$m = 1,2,...,N$$

$$n = 1,2,...,N \tag{2.38}$$

The system of equations given in Eq. 2.35 can be written in matrix form as

$$[Z_{mn}][I_n] = \left[V_m^P\right] \tag{2.39}$$

where $[I]$ is the generalized current column vector whose N components contain the I_n of Eq. 2.22, $[Z_{mn}]$ is the NxN generalized impedance matrix, and $\left[V_m^P\right]$ is the generalized voltage column vector. The dimensions of the elements Z_{mn} and V_m^P are volt-amperes (VA), while the elements I_n are dimensionless.

2.2 Calculation of the Generalized Voltage Matrix $\left[V_m^P\right]$

If the dipole is excited by a delta-gap generator, the evaluation of the voltage vector elements V_m^P given by Eqs. 2.37 is simple: only these position in the generalized voltage matrix corresponding to segment junction that contain the generator will have non zero value (V_m^P =1 for a delta-gap generator of 1V) (Lo *et al.*, 1977).

When the dipole is excited by a probe, the evaluation of V_m^P is rather involved. In this case, we need to find $\bar{E}_m(x,y,z)$ which is the electric field in the dielectric layer (2) due to the m^{th} expansion mode $\bar{f}_m(x,y)$ of the surface current density on the dipole.

If the impressed source is assumed to be an idealized current source (probe feed) expressed as:

$$\bar{J}^{(i)}(x,y,z) = \hat{z}\,\delta(x-x_p)\,\delta(y-y_p) \tag{2.40}$$

where the feed position is at (x_p,y_p). The voltage vector elements reduce to

$$V_m^P = \iiint \bar{E}_m(x,y,z)\cdot\hat{z}\,\delta(x-x_p)\,\delta(y-y_p)dV = \int_{-h_2}^{0} \bar{E}_{zm}(x_p,y_p,z)\,dz \tag{2.41}$$

where E_{zm} is the z-component of $\bar{E}_m$.

Using the dyadic Green's function formulation, we have

$$\bar{E}_m(x,y,z) = i\omega \iint_{S_m} \bar{\bar{G}}_{21}(\bar{r},\bar{r}_s') \cdot \bar{f}_m(\bar{r}_s') dS' \quad (2.42)$$

where $\bar{\bar{G}}_{21}(\bar{r},\bar{r}_s')$ is the dyadic Green's function in layer (2) due to a point source in layer (1) on the dipole surface.

$\bar{\bar{G}}_{21}(\bar{r},\bar{r}_s')$ for the layered uniaxially anisotropic medium can be given as:

$$\bar{\bar{G}}_{21}(\bar{r},\bar{r}')\Big|_{z'=0} = \int_{-\infty}^{\infty}\int d\bar{k}_s \; e^{i\bar{k}_s\cdot(\bar{r}_s-\bar{r}_s')} \; \bar{\bar{g}}_{21}(\bar{k}_s,z) \quad (2.43)$$

where

$$\bar{g}_{21}(\bar{k}_s,z) = \frac{i\mu_0}{8\pi^2}\left\{\frac{r_1^{TE}}{k_{1z}^{(h)}} X_{\cap 2,1}^{TE}\left[\hat{h}\left(-k_{2z}^{(h)}\right)e^{-ik_{2z}^{(h)}z} + R_{\cap 2}^{TE} e^{2ik_{2z}^{(h)}h_2}\,\hat{h}\left(k_{2z}^{(h)}\right)e^{ik_{2z}^{(h)}z}\right]\left[\hat{h}\left(-k_{1z}^{(h)}\right) + R_{\cup 1}^{TE} e^{2ik_{1z}^{(h)}h_1}\,\hat{h}\left(k_{1z}^{(h)}\right)\right] + \frac{r_1^{TM}}{k_{1z}^{(e)}} X_{\cap 2,1}^{TM}\left[\hat{v}\left(-k_{2z}^{(e)}\right)e^{-ik_{2z}^{(e)}z} + R_{\cap 2}^{TM} e^{2ik_{2z}^{(e)}h_2}\,\hat{v}\left(k_{2z}^{(e)}\right)e^{ik_{2z}^{(e)}z}\right]\left[\hat{v}\left(-k_{1z}^{(e)}\right) + R_{\cup 1}^{TM} e^{2ik_{2z}^{(e)}h_1}\,\hat{v}\left(k_{1z}^{(e)}\right)\right]\right\} \quad (2.44)$$

where

$$X_{\cap 2,1}^{TE} = \frac{\left(1+R_{\cap 1}^{TE}\right)}{\left(1+R_{\cap 2}^{TE}\,e^{2ik_{2z}^{(h)}h_2}\right)} \quad (2.45)$$

$$X_{\cap 2,1}^{TM} = \frac{k_2}{k_{2z}^{(e)}}\,\frac{k_{1z}^{(e)}}{k_1}\,\frac{\left(1-R_{\cap 1}^{TM}\right)}{\left(1-R_{\cap 2}^{TM}\,e^{2ik_{2z}^{(e)}h_2}\right)} \quad (2.46)$$

$$R_{\cap 2}^{TE} = -1 \quad R_{\cap 2}^{TM} = 1$$

Since $\bar{f}_m(x,y)$ is assumed to be x-directed in Eq 2.22, and it is required to evaluate only the z-component of the electric field E_{zm}. Thus,

$$E_{zm}(x_p,y_p,z) = i\omega \iint_{S_m} \bar{\bar{G}}_{21}^{(z,x)}(x_p,y_p,z,\bar{r}_s')\cdot f_m(\bar{r}_s')dS' \quad (2.47)$$

where the (z,x) component only of the dyadic Green's function $G_{21}^{(z,x)}$ is required.

Using Eq. 2.44, Eq. 2.15 and Eq. 2.16 $g_{21}^{(z,x)}$ can be obtained as

$$g_{21}^{(z,x)}(\bar{k}_s,z) = \frac{i\mu_0}{8\pi^2}\,\frac{\varepsilon_2}{\varepsilon_{2z}}\,\frac{r_1^{TM}}{k_1 k_2}\,X_{\cap 2,1}^{TM}\,k_x\left(1-R_{\cup 1}^{TM}\,e^{2ik_{1z}^{(e)}h_1}\right)\left(e^{-ik_{2z}^{(e)}z} + R_{\cap 2}^{TM}\,e^{2ik_{2z}^{(e)}h_2}\,e^{ik_{2z}^{(e)}z}\right) \quad (2.48)$$

where the TE- components do not contribute.

From Eq. 2.43, Eq. 2.47 and Eq. 2.48, the expression for E_{zm} reduces to:

$$E_{zm}(x_p,y_p,z) = i\omega \iint_{S_m} dx'\,dy' \int_{-\infty}^{\infty}\int d\bar{k}_s \; e^{i(\bar{k}_x x_p + \bar{k}_y y_p)} \; g_{21}^{(z,x)}(\bar{k}_s,z)\,e^{i\bar{k}\cdot\bar{r}_s'} f_m(\bar{r}_s') \quad (2.49)$$

Since

$$\iint_{S_m} dx'dy' \; e^{i\bar{k}_s\cdot\bar{r}_s'} \; f_m(\bar{r}_s') = \tilde{F}_m(k_s) \quad (2.50)$$

thus

$$E_{zm}(x_p,y_p,z) = i\omega \int_{-\infty}^{\infty}\int dk_x\,dk_y \; e^{i(k_x x_p + k_y y_p)} \; g_{21}^{(z,x)}(\bar{k}_s,z)\,\tilde{F}_m(\bar{k}_s) \quad (2.51)$$

Substituting Eq. 2.51 in Eq. 2.41, we arrive at

$$V_m^P = i\omega \int_{-\infty}^{\infty}\int dk_x\,dk_y \; e^{i(k_x x_p + k_y y_p)} \; \tilde{F}_m(\bar{k}_x,\bar{k}_y)\cdot g_{21(I)}^{(z,x)}(k_x,k_y,z),$$

m=1,2,....,N

where

$$g_{21(I)}^{(z,x)} = \int_{-h_2}^{0} g_{21}^{(z,x)}(k_x,k_y,z)\,dz = -\frac{\mu_0}{8\pi^2}\,\frac{\varepsilon_2}{\varepsilon_{2z}}\,\frac{r_1^{TM}}{k_1^2}\,\frac{k_{1z}^{(e)}}{\left(k_{2z}^{(e)}\right)^2}\,k_x\left(1-R_{\cap 1}^{TM}\right)\left(1-R_{\cup 1}^{TM}\,e^{2ik_{1z}^{(e)}h_1}\right) \quad (2.52)$$

The Z_{mn} and V_m^P appearing in Eq. 2.38 and Eq. 2.51, respectively have to be computed using numerical integration techniques and properly accounting for the residue contribution of the surface wave poles. The unknown complex coefficients I_n are determined after solving Eq. 2.39.

2.3 Calculation of Input Impedance

For the case when the dipole is excited by delta-gap generator, the input impedance may be found from $Z_{in} = \frac{V_{in}}{I_{in}}$. So, if $V_{in} = 1$, the input impedance is simply $Z_{in} = \frac{1}{I_{in}}$.

For a dipole excited by a probe, the input impedance can be calculated as:

$$Z_{in} = -\sum_{n=1}^{N} I_n V_n^P \quad (2.53)$$

where I_n are the expansion mode current amplitudes and I is the probe current.

2.4 Computational Efficiency

Because of the computational complexity of Eq. instead of performing the doubly infinite integrals in the (k_x,k_y) space, it is common to change to polar coordinates (k) in the spectral domain, where

$k_x = k \cos$ (2.54)

$k_y = k \sin$ (2.55)

In this case, the integrations in Eq. 2.38 and Eq. 2.52 undergo a transformation which can be symbolically shown as

$$\int_{-\infty}^{\infty}\int U(k_x,k_y)\,dk_x\,dk_y = \int_0^{2p} d\alpha \int_0^{\infty} dk_\rho\, k_\rho\, U(k_\rho,\alpha) \quad (2.56)$$

Thus, the doubly infinite integrals are reduced to a finite integration and a semi-infinite integration. Also, the even and odd properties of the integrands can be used to reduce the $\alpha = 0 \to 2\pi$ integration range to $\alpha = 0 \to \frac{\pi}{2}$. Eq 2.38 and Eq. 2.52 can then be written as

$$Z_{mn} = -4i\omega \int_0^{\pi/2} d\alpha \int_0^{\infty} dk_\rho\, k_\rho\, g_{11}^{(x,x)}\left(k_\rho,\alpha\right) \cdot \mathrm{Re}\left\{\tilde{\Phi}_n^*\,\tilde{\Phi}_m\right\} \cdot \mathrm{Re}\left\{\tilde{\Psi}_n^*\,\tilde{\Psi}_m\right\}$$

$m = 1,2,\ldots,N$

$n = 1,2,\ldots,N$ (2.57)

and

$$V_m = -4\omega \int_0^{\pi/2} d\alpha \int_0^{\infty} dk_\rho k_\rho\; g_{21}^{(z,x)}\left(k_\rho,\alpha\right) \mathrm{Im}\left\{\tilde{\Phi}_m\, e^{ik_x x_p}\right\} \cdot \mathrm{Re}\left\{\tilde{\Psi}_n\, e^{ik_y y_p}\right\},$$

m=1,2,..., N (2.58)

The integrals in Eq. 2.57 and Eq. 2.58 are to be evaluated numerically. Thus, the expressions for Z_{mn} and V_m constitute the bulk of the computational effort for the microstrip dipole solution, and so it is critical that these terms be calculated as efficiently as possible. The singularities of the integrand correspond to TM and TE surface waves. If the dielectric layers are lossless, then the surface wave poles are on the $\mathrm{R_e}\{k\}$ axis between k_0 and k_j, where $k_j = \sqrt{\varepsilon_j}\, k_0$ is the wave number in the dielectric layer with higher dielectric constant. As illustrated in Figure 2.2, if the dielectrics are lossy, then the poles move in the third quadrant. However, for low-loss dielectrics, the poles are very close to the $\mathrm{R_e}\{k\}$ axis. These poles must be avoided in performing the numerical integration from k=0 to. The conventional method of avoiding the poles is to deform the contour from the $\mathrm{R_e}\{k\}$ axis to the contour C_1 which makes a small half-circle around each pole.

The integrals around the half-circle can be done in closed form by computing the residues at the poles. This method works well for one layer structure and when the substrate is electrically thin, there is only one surface wave pole (TM surface wave pole). However, for multilayered structure (or if the substrate is not electrically thin), there can be several surface wave poles. Also, analytically performing the integrations around the half-circles will be complicated if two or more poles are extremely close to each other. These problems can be entirely avoided by deforming the contour C_1 into the contour C_2.

The contour C_2 goes down from the origin at 45° angle until it is at height $-jH$ below the $\mathrm{R_e}\{k\}$ axis. It is then proceeded parallel to the $\mathrm{R_e}\{k\}$ axis until it is past k_j. Finally, it moves back up to the $\mathrm{R_e}\{k\}$ axis and then out to . The advantage of the contour C_2 is that numerical integration near the poles is avoided. Further, no knowledge of the pole locations or their number is required. This method works well for H on the order of $0.1k_0$ (Derneryd, 1977, Carver, 1979). If the dipole is divided into equal-length segments, all the values of the N^2 matrix elements are contained in any one row of [Z_{mn}], say the first one.

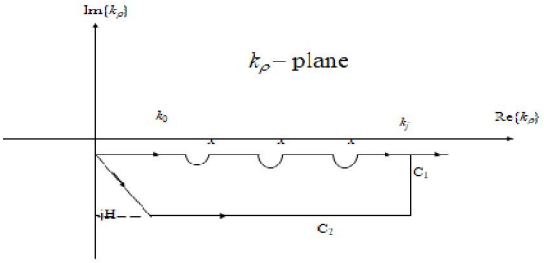

Figure 2.2. Two paths of integration in the complex k -plane

All other rows are morally a rearranged version of the first. The remaining elements can be obtained by the rearrangement algorithm (Lo *et al.,* 1977)

$Z_{mn} = Z_{1,|m-n|+1}$, $m \geq 2$, $n \geq 1$, (2.59)

Such a matrix is said to be a toeplitz matrix. In this case execution time is considerably reduced from:

$t \cong A N^2 + BN^3$ (2.60)

to

$t \cong A N + BN^{5/3}$ (2.61)

where A is the time required to compute a typical impedance matrix element, $B N^3$ is the time required to solve $[Z_{mn}][I_n] = [V_m]$ for $[I_n]$ by matrix inversion for a system of order N, where $[Z_{mn}]$ is a non-teoplitz matrix. This time is reduced to $BN^{5/3}$ by using a computer program for solving the teoplitz matrix.

2.5 Radiation Field Evaluation

The current distribution is radiating in the presence of the layered anisotropic medium. To find the field patterns, the expression for electric and magnetic field is obtained in the upper half-space. Using the dyadic Green's function in the upper half-space due to the current distribution on the dipole. These fields are represented in terms of Sommerfeld-Weyl-type integrals. These integrals are calculated in the radiation zone or far-field region. Such integrals can be evaluated with numerical integration routines, but it becomes very tedious when observation point is in the far field of the source, because the integrand is rapidly oscillating. However, in the far-field region, we can use the stationery phase method or the saddle point method to evaluate the integral to obtain far-field expressions. Here a method that captures the essence of the stationary phase method is presented and the far field approximations of the Sommerfeld-weyl type integrals are derived. The result of this calculation is correct asymptotically to the leading-order which we are interested in.

2.6 The Electric and Magnetic Fields in the Upper-Half-space

In the upper-half space (region 0), the far-field satisfies the following relations:

$$E_{0\theta} = -\frac{E_{0z}}{\sin\theta} \quad (2.62)$$

$$H_{0\phi} = \frac{1}{\eta_0} E_{0\theta} \quad (2.63)$$

for TM waves, and

$$H_{0\theta} = -\frac{H_{0z}}{\sin\theta} \quad (2.64)$$

$$E_{0\phi} = -\eta_0 H_{0\theta} \quad (2.65)$$

for TE waves, and

$$\eta_0 = \sqrt{\frac{\mu_0}{\varepsilon_0}} \quad (2.66)$$

Thus, to calculate the far-field expressions we need to calculate E_{0z} and H_{0z} in the upper half space (layer(0)) due to the current distribution $\bar{J}_s(\bar{r}') = \hat{x} J_x(x', y')$ on the microstrip dipole in layer (1).

The electric field E_{0z} can be obtained as

$$E_{0z} = \hat{z} \cdot \bar{E}_0 = \hat{z} \cdot i \iint_{S'} dr' \, \overline{\overline{G}}_{01}(\bar{r}, \bar{r}') \cdot \bar{J}_s(\bar{r}')$$

$$= i \iint_{S'} dx' \, dy' \, G_{01}^{(z,x)}(\bar{r}, \bar{r}') \, J_x(x', y') \quad (2.67)$$

where

$$G_{01}^{(z,x)}(\bar{r}, \bar{r}') = \hat{z} \cdot \overline{\overline{G}}_{01}(\bar{r}, \bar{r}') \cdot \hat{x} \quad (2.68)$$

$\overline{\overline{G}}_{01}(\bar{r}, \bar{r}')$ can be obtained as (See Figure. 2.3). and $\bar{r}'$ in region (1) where $z' = -h_1$

$$G_{01}^{(z,x)}(\bar{r}, \bar{r}') = \int_{-\infty}^{\infty} \int dk_x \, dk_y \, e^{i\bar{k}_s \cdot (\bar{r}_s - \bar{r}_s')} \, g_{01}^{(z,x)}(\bar{k}_s, z, z') \quad (2.69)$$

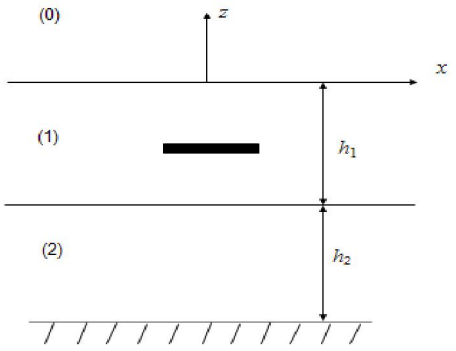

Figure 2.3, Geometry of problem with sources in region(1) and observation point in region (0).

For the case of uniaxially anisotropic medium,

$$G_{01}^{(z,x)}(\bar{r}, \bar{r}') = \int_{-\infty}^{\infty} \int dk_x \, dk_y \, e^{i\bar{k}_s \cdot (\bar{r}_s - \bar{r}_s')} \, g_{01}^{(z,x)}(\bar{k}_s, z, z')$$

where

$$g_{01}^{(z,x)}(\bar{k}_s, z, z') = \frac{i\mu_0}{8\pi^2} \cdot \frac{r_1^{TM}}{k_{1z}^{(e)}} X_{\cup 0,1}^{TM} \, \hat{z} \cdot \left\{ \hat{v}(k_{0z}) e^{ik_{0z} z} \left[\hat{v}\left(k_{1z}^{(e)}\right) e^{-k_{1z}^{(e)} z'} + R_{\cap 1}^{TM} e^{2ik_{1z}^{(e)} h_1} \hat{v}\left(-k_{1z}^{(e)}\right) e^{ik_{1z}^{(e)} z'} \right] \right\} \cdot \hat{x} \quad (2.70)$$

where in our case $z' = -h_1$ since the dipole is on the boundary between layers (1) and (2), and

$$r_1^{TM} = \frac{1}{1 - R_{\cap 1}^{TM} R_{\cup 1}^{TM} e^{2ik_{1z}^{(e)} h_1}} \quad (2.71)$$

$$R_{\cup 1}^{TM} = R_{10}^{TM} \quad (2.72)$$

$$X_{\cup 0,1}^{TM} = \frac{k_0}{k_{0z}} \frac{k_{1z}^{(e)}}{k_1} \left(1 - R_{\cup 1}^{TM}\right) \quad (2.73)$$

performing the dot product in Eq. 2.70, we get

$$g_{01}^{(z,x)}(\bar{k}_s, z) = \frac{-i\mu_0}{8\pi^2} \frac{r_1^{TM}}{k_0} X_{\cup 0,1}^{TM} e^{ik_{0z}z} e^{ik_{1z}^{(e)} h_1} \frac{k_x}{k_1} \left(1 - R_{\cap 1}^{TM} e^{ik_{1z}^{(e)} h_1}\right) \quad (2.74)$$

where z' is substituted by ($-h_1$).

Thus, the z-component of the electric field in region (0) is given by

$$E_{0z}(\bar{r}) = \frac{\omega\mu_0}{8\pi^2} \iint_{S'} dx'\, dy'\; J_x(x', y') (-i) \frac{\partial}{\partial x} \int_{-\infty}^{\infty} \int d\bar{k}_s \; e^{i\left[k_x (x - x') + k_y (y - y')\right]} e^{ik_{0z}z} \; g_E(\bar{k}_s) \quad (2.75)$$

where

$$g_E(\bar{k}_s) = \frac{r_1^{TM}}{k_0 k_1} X_{\cup 0,1}^{TM} e^{ik_{1z}^{(e)} h_1} \left(1 - R_{\cap 1}^{TM} e^{ik_{1z}^{(e)} h_1}\right) \quad (2.76)$$

and k_x is taken outside the integral as $(-i)\frac{\partial}{\partial x}$. Thus, E_{0z} is obtained and expressed in Eq. 2.75 in terms of Weyl-type integral. E_{0z} can also be expressed in terms of a Sommerfeld-type integral as

$$E_{0z} = (i)\frac{\omega\mu_0}{4\pi} \cdot \iint_{S'} dx'\, dy'\; J_x(x', y') \cos\phi \cdot \int_0^{\infty} dk_\rho \; k_\rho^2 g_E(k_\rho) \, e^{ik_{0z}z} J_1\left(k_\rho \left|\bar{\rho} - \bar{\rho}'\right|\right) \quad (2.77)$$

where we used the relation

$$\frac{\partial}{\partial x} J_0\left(k_\rho \left|\bar{\rho} - \bar{\rho}'\right|\right) = -\cos\phi \; k_\rho \, J_1\left(k_\rho \left|\bar{\rho} - \bar{\rho}'\right|\right) \quad (2.78)$$

The magnetic field in the upper half-space can be obtained from Maxwell's equations

$$\bar{H}_0 = \frac{1}{i\omega\mu_0} \nabla \times \bar{E}_0 \quad (2.79)$$

That is

$$\bar{H}_0(\bar{r}) = \frac{1}{\mu_0} \iint_{S'} dx'\, dy' \, \nabla \times \bar{\bar{G}}_{01}(\bar{r}, \bar{r}') \cdot \bar{J}_s(x', y') \quad (2.80)$$

where

$$\bar{\bar{G}}_{01}(\bar{r}, \bar{r}') = \frac{i\mu_0}{8\pi^2} \int \int_{-\infty}^{\infty} d\bar{k}_s \; e^{i\bar{k}_s \cdot (\bar{r}_s - \bar{r}_s')} \; e^{ik_{0z}z} \left\{ \frac{r_1^{TE}}{k_{1z}^{(h)}} X_{\cup 0,1}^{TE} e^{ik_{1z}^{(h)} h_1} \hat{h}(k_{0z}) \left[\hat{h}\left(k_{1z}^{(h)}\right) + R_{\cap 1}^{TE} e^{ik_{1z}^{(h)} h_1} \hat{h}\left(-k_{1z}^{(h)}\right)\right] \right\} + \frac{r_1^{TM}}{k_{1z}^{(e)}} X_{\cup 0,1}^{TM} e^{ik_{1z}^{(e)} h_1} \hat{v}(k_{0z}) \left[\hat{v}\left(k_{1z}^{(e)}\right) + R_{\cap 1}^{TM} e^{ik_{1z}^{(e)} h_1} \hat{v}\left(-k_{1z}^{(h)}\right)\right] \quad (2.81)$$

Performing the curl operation, so:

$$\nabla \times \bar{\bar{G}}_{01}(\bar{r}, \bar{r}') = \frac{i\mu_0}{8\pi^2} \int \int_{-\infty}^{\infty} d\bar{k}_s \; e^{i\bar{k}_s \cdot (\bar{r}_s - \bar{r}_s')} \; e^{ik_{0z}z'} \left\{ \frac{r_1^{TE}}{k_{1z}^{(h)}} X_{\cup 0,1}^{TE} e^{ik_{1z}^{(h)} h_1} (-ik_0) \hat{v}(k_{0z}) \left[\hat{h}\left(k_{1z}^{(h)}\right) + R_{\cap 1}^{TE} e^{ik_{1z}^{(h)} h_1} \hat{h}\left(-k_{1z}^{(h)}\right)\right] \right\} + \frac{r_1^{TM}}{k_{1z}^{(e)}} X_{\cup 0,1}^{TM} e^{ik_{1z}^{(e)} h_1} (ik_0) \hat{h}(k_{0z}) \left[\hat{v}\left(k_{1z}^{(e)}\right) + R_{\cap 1}^{TM} e^{ik_{1z}^{(e)} h_1} \hat{v}\left(-k_{1z}^{(e)}\right)\right] \quad (2.82)$$

Hence, the magnetic field H_{0z} can be obtained as

$$H_{0z} = \hat{z} \cdot \bar{H}_0 = \frac{1}{\mu_0} \iint_{S'} dx'\, dy' \, \hat{z} \cdot \left(\nabla \times \bar{\bar{G}}_{01}\right) \cdot \hat{x} J_x(x', y') \quad (5.22)$$

$$H_{0z} = \frac{i}{8\pi^2} \iint_{S'} dx'\, dy' \, J_x(x', y')$$

$$(-i)\frac{\partial}{\partial y}\int_{-\infty}^{\infty}\int d\bar{k}_s \; e^{i\left[k_z(x-x')+k_z(y-y')\right]}\, e^{ik_{0z}z}\; g_H(\bar{k}_s) \tag{2.83}$$

where

$$g_H(\bar{k}_s) = \frac{r_1^{TE}}{k_{1z}^{(h)}}\, X_{\cup 0,1}^{TE}\, e^{ik_{1z}^{(h)}h_1}\left(1+R_{\cap 1}^{TE}e^{ik_{1z}^{(h)}h_1}\right) \tag{2.84}$$

where

$$r_1^{TE} = \frac{1}{1-R_{\cap 1}^{TE}R_{\cup 1}^{TE}e^{2ik_{1z}^{(h)}h_1}} \tag{2.85}$$

$$R_{\cup 1}^{TE} = R_{10}^{TE} \tag{2.86}$$

$$X_{\cup 0,1}^{TE} = \left(1+R_{\cup 1}^{TE}\right) \tag{2.87}$$

Thus, H_{0z} is obtained and expressed in terms of Weyl-type integral. In a similar way, H_{0z} can be expressed in terms of a Sommerfeld type integral as

$$H_{0z} = \frac{-1}{4\pi}\iint_{S'} dx'\,dy'\; J_x(x',y') \sin\phi \cdot \int_0^{\infty} dk_\rho\, k_\rho^2 g_H(k_\rho)\, e^{ik_{0z}z}\cdot J_1\left(k_\rho\,|\bar{\rho}-\bar{\rho}'|\right) \tag{2.88}$$

where the relation

$$\frac{\partial}{\partial y}\, J_0\left(k_\rho\,|\bar{\rho}-\bar{\rho}'|\right) = -\sin\phi\;\; J_1\left(k_\rho\,|\bar{\rho}-\bar{\rho}'|\right) \tag{2.89}$$

Can be written.

2.7 Leading-Order Approximations to Sommerfeld-Weyl-Type Integrals

Let us consider an integral of the type

$$I = \int_{-\infty}^{\infty} d\lambda\; g(\lambda,\Omega) \tag{2.90}$$

where is a large parameter. If the integrand becomes rapidly oscillating when is large, and it there exists a simple stationary phase point in the integrand, we can evaluate a leading order approximation of Eq. 5.30 using the method of stationary phase (Lo et al., 1979).

The first step in the procedure is to factorize the integrand g(,) into two parts, a slowly varying part and a rapidly varying part. So, we let

$$I = \int_{-\infty}^{\infty} d\lambda \quad f(\quad)\,h(\quad,\quad) \tag{2.91}$$

where $f(\quad)$ is the slowly varying part, while $h(\quad,\quad)$ is the rapidly varying part when ∞. Assuming here that $h(\quad,\quad)$ is of the form

$$h(\quad,\quad) = e^{i\quad s(} \tag{2.92}$$

Next, finding the stationary phase point of $h(\quad,\quad)$ which is given by the value of where

$$\left.\frac{\partial S(\lambda)}{\partial(\lambda)}\right|_{\lambda=\lambda_0} = 0 \tag{2.93}$$

Most of the contributions to the integral in Eq. 5.31 will be from the vicinity of the stationary phase point. Hence, replacing the slowly varying part of the integrand $f(\quad)$ by its value at the stationary phase point. By so doing, Eq. 2.91 becomes

$$I \sim f(\quad)\int_{-\infty}^{\infty} d\lambda \quad h(\quad,\quad), \qquad \infty \tag{2.94}$$

If the integral has a closed-form expression, Eq. 2.94 is an analytic expression for the leading-order approximation of Eq.2.90. An illustration of how the foregoing method is applied to find the far-field approximations of Sommerfeld-Weyl-type integrals.

The following two identities are used in this approximation:

1) The Weyl Identity (Richards and Lom 1981): so

$$\frac{e^{ikr}}{r} = \frac{i}{2\pi}\int_{-\infty}^{\infty}\int dk_x\, dk_y\; \frac{e^{i\left[k_x x+k_y y+k_z|z|\right]}}{k_z} \tag{2.95}$$

2) The Sommerfeld Identity (Richards and Lom 1981): thus

$$\frac{e^{ikr}}{r} = \frac{i}{2}\int_{-\infty}^{\infty} dk_\rho\; \frac{k_\rho}{k_z} H_0^{(1)}\left(k_\rho\rho\right) e^{ik_z|z|} \tag{2.96}$$

In Eq.2.95, $k_z = \sqrt{k^2 - k_x^2 - k_y^2}$, and in Eq. 2.96 $k_z = \sqrt{k^2 - k_\rho^2}$

Let as consider first a Weyl-type integral in the form we encountered for the fields in the upper half-space as

$$I_1 = \int_{-\infty}^{\infty}\int dk_x\, dk_y\; g\left(k_x,k_y\right)\; e^{i\left[k_x x+k_y y+k_z|z|\right]} \tag{2.97}$$

where k_z is defined in Eq. 2.95. When x, y, or z are large, the integrand in Eq. 2.97 is rapidly oscillating, and the integral is amenable to the stationary phase approximation. With the Weyl identity in mind, factorizing the integrand into slowly

varying part and a rapidly varying part which can be integrated in closed form; that is, writing

$$I_1 = \int_{-\infty}^{\infty}\int dk_x\, dk_y \left\{ g(k_x, k_y)\, k_z \right\} \left\{ \frac{e^{i\left[k_z x + k_y y + k_z |z|\right]}}{k_z} \right\} \quad (2.98)$$

By virtue of the stationary phase method argument, contributions to the integral will come from around the point where the phase of the exponential function is stationary. Hence, looking for the stationary phase point in the two-dimensional k_x-k_y space which is given by

$$\frac{\partial}{\partial k_x}\, i\left(k_x x + k_y y + k_z |z|\right) = 0,$$
$$\frac{\partial}{\partial k_y}\, i\left(k_x x + k_y y + k_z |z|\right) = 0 \quad (2.99)$$

This is easily solvable to give the stationary phase point at

$$k_{x0} = k\,\frac{x}{r}\,,\; k_{y0} = k\,\frac{y}{r} \quad (2.100)$$

where $r = \sqrt{x^2 + y^2 + z^2}$. Eq. 2.97 or Eq. 2.98 can be physically interpreted as expansions in a spectrum of plane waves. The physical interpretation of the stationary phase point, as expressed by Eq. 2.100, is that only the plane wave whose $\bar{k}$ -vector $\left(\bar{k} = \hat{x}k_x + \hat{y}k_y + \hat{z}k_z\right)$ points from the source point to the observation point is important in evaluating the field at the observation point. By replacing the slowly varying part of the integrand in Eq. 2.98 with its value at the stationary phase point, getting:

$$I_1 \sim \mathrm{g}(k_{x0}, k_{y0})\, k_{z0} \int_{-\infty}^{\infty}\int dk_x\, dk_y\, \frac{e^{i(k_x x + k_y y + k_z |z|)}}{k_z}, \quad r \to \infty \quad (2.101)$$

Using Weyl identity, Eq. 2.101 can be evaluated in closed form to obtain the leading-order approximation to the integral as

$$I_1 \sim -2i\; \mathrm{g}(k_{x0}, k_{y0})\, k_{z0}\, \frac{e^{ikr}}{r}, \quad r \to \infty \quad (2.102)$$

where

$$k_{0z} = \sqrt{k^2 - k_{x0}^2 - k_{y0}^2} = k|z|/r.$$

Let us next consider a Sommerfeld-type integral of the form

$$I_2 = \int_{-\infty}^{\infty} dk_\rho\, k_\rho\, g_n(k_\rho)\, J_n(k_\rho \rho)\, e^{ik_z|z|} \quad (2.103)$$

Where k_z is defined following Eq. 2.96. When ∞, using the large argument approximation for the Bessel function, notice that the integrand does not have a well-defined stationary phase point. To obtain an integrand with the form of Eq. 2.96, it is most appropriate to convert the above integral from a semi-infinite integral to an infinite integral and replace the Bessel function with a Hankel function. This will lead to the use of the Sommerfeld identity given in Eq. 2.96.

Before proceeding any further, notice that Eq. 2.103 is also obtained when writing Eq. 2.97 in terms of cylindrical coordinates by letting

$$k_x = k\cos, \; k_y = k\sin, \; x = \cos\phi, \; y = \sin\phi \quad (2.104)$$

Then Eq. 2.97 becomes

$$I_1 = \int_0^{\infty} dk_\rho\, k_\rho \int_0^{2\pi} d\alpha\, \hat{g}(k_\rho, \alpha)\, e^{ik_\rho \rho \cos(\alpha - \phi) + ik_z|z|} \quad (2.105)$$

where $\hat{\mathrm{g}}(k\quad) = g(k\quad\cos\quad k\quad\sin)$.

Next, $\hat{\mathrm{g}}(k)$ can be expanded in Fourier series in the -variable as:

$$\hat{\mathrm{g}}(k\quad) = \sum_{n=-\infty}^{\infty} e^{in\alpha}\, \hat{g}_n(k_\rho) \quad (2.106)$$

Substituting back Eq. 2.106 into Eq. 2.105 and making use of the following integral identity for the Bessel function

$$J_n(k) = \frac{1}{2\pi}\int_0^{2\pi} \mathrm{d}\alpha\; e^{ik_\rho \rho \cos\alpha + in\alpha - in\pi/2} \quad (2.107)$$

Obtaining

$$I_1 = \sum_{n=-\infty}^{\infty} 2\pi\, e^{in\phi + in\pi/2} \int_0^{\infty} dk_\rho\, k_\rho \hat{g}_n(k_\rho)\, J_n(k)\, e^{ik_z|z|} \quad (2.108)$$

Now identity each term in the series to be similar to Eq. 2.103. From Eq. 2.106, if we denote $(k_x k_y)$ by (k) in cylindrical coordinates, then the point $(-k_x, -k_y)$ can be denoted by (k) or $(-k_\rho)$. Because of this, deduce that

$$\hat{g}_n(-k_\rho) = e^{in}\quad \hat{g}_n(k) \quad (2.109)$$

Hence the function $g_n(k\ )$ in Eq. 2.103 which is similar to $\hat{g}_n(k\ )$ in general has the above property. Next, by using the identity for Bessel functions in terms of Hankel functions,

i.e. $J_n(x) = \frac{1}{2}\left[H_n^{(1)}(x) + H_n^{(2)}(x)\right]$ (Abramowitz and Stegun, 1986), writing Eq. 2.103 as

$$I_2 = \frac{1}{2}\int_0^\infty dk_\rho\ k_\rho g_n\left(k_\rho\right)\ H_n^{(1)}\left(k_\rho\rho\right)\ e^{ik_z|z|} + \frac{1}{2}\int_0^\infty dk_\rho\ k_\rho g_n\left(k_\rho\right)\ H_n^{(2)}\left(k_\rho\rho\right)\ e^{ik_z|z|} \quad (2.110)$$

With the change of variables from k to k'_ρ for the second integral, the use of the property of the Hankel function that

$\mathrm{H}_n^{(2)}\left(x\ e^{-i\pi}\right) = -\mathrm{e}^{-in\pi}\ H_n^{(1)}(x)$ [13], and the property for $g_n(k\ )$ given by Eq. 2.109, combining the two integrals in Eq. 2.110 into one integral as

$$I_2 = \frac{1}{2}\int_{-\infty}^\infty dk_\rho\ k_\rho g_n\left(k_\rho\right)\ H_n^{(1)}\left(k_\rho\rho\right)\ e^{ik_z|z|} \quad (2.111)$$

The integrand in Eq. 2.111 is rapidly oscillating when or z tends to ∞ because

$$\mathrm{H}_n^{(1)}(x) \sim \sqrt{\frac{2}{\pi x}}\ \mathrm{e}^{i\left(x-n\pi/2-\pi/4\right)} \quad (2.112)$$

when $x\ \infty$ (Newman and Tulyathan, 1981). Next factorizing the integrand in Eq. 2.111 into two parts so that Sommerfeld identity can be used in Eq. 2.96. Consequently,

$$I_2 = \frac{1}{2}\int_{-\infty}^\infty dk_\rho \left\{ g_n\left(k_\rho\right)\frac{H_n^{(1)}(k_\rho\rho)}{H_0^{(1)}(k_\rho\rho)}k_z \right\} \left\{ \frac{k_\rho}{k_z} H_0^{(1)}\left(k_\rho\rho\right)k_z e^{ik_z|z|} \right\} \quad (2.113)$$

In view of Eq. 2.112, the first factor in Eq. 2.113 is slowly varying while the second factor is rapidly varying when $r\ \infty$ (i.e. when the observation point is far from the field point). Since the rapidly varying part of the integrand is asymptotic to the phase factor $e^{ik_\rho\rho+ik_z|z|}$, the location the stationary phase point is given by

$$\frac{\partial}{\partial k_\rho}\ i\left(k_\rho\rho + k_z|z|\right)\Big|_{k_{\rho 0}} = 0 \quad (2.114)$$

The solution of Eq. 2.114 is

$k_{\rho_0} = k\sin$, $k_{z0} = k\cos$ (2.115)

With = $\sin^{-1}($ r , as the angle of the observation point with respect to source point. Now evaluating the slowly varying part of the integrand at the stationary point and use Sommerfeld identity to evaluate the rapidly varying part in closed form.

As a result

$$I_2 \sim -i\ g_n\left(k_{\rho_0}\right)\frac{H_n^{(1)}(k_{\rho_0}\rho)}{H_0^{(1)}(k_{\rho_0}\rho)}k_{z0}\ \frac{e^{ikr}}{r}, \quad r\to\infty \quad (2.116)$$

When $r\to\infty$, using the large argument approximation of the Hankel function to simplify

$$\frac{H_n^{(1)}\left(k_\rho\rho\right)}{H_0^{(1)}\left(k_\rho\rho\right)} \sim e^{in\pi/2},\ k_\rho\rho\to\infty \quad (2.117)$$

Hence Eq. 2.116 is simplified to

$$I_2 \sim (-i)^{n+1}\ g_n\left(k_{\rho_0}\right)k_{z0}\ \frac{e^{ikr}}{r},\ r\to\infty \quad (2.118)$$

2.8 Far-Field Expressions

The results obtained in section Eq.2.63 are applied to find the far-field expressions.

The z- component of the electric field in the upper half-space given by Eq. 2.77, can be written as

$$E_{0z}(\bar{r}\ ) = \frac{i\omega\mu_0}{4\pi}\iint_{S'} dx'\ dy'\ J_x(x',y')\cos\phi\ I_E \quad (2.119)$$

where

$$I_E = \int_0^\infty dk_\rho\ k_\rho^2\ g_E\left(k_\rho\right)\ e^{ik_{0z}z}\ J_1\left(k_\rho|\bar{\rho}-\bar{\rho}'|\right) \quad (2.120)$$

which can be put in the form

$$I_E = \frac{1}{2}\int_{-\infty}^\infty dk_\rho\ k_\rho^2\ g_E\left(k_\rho\right)\ e^{ik_{0z}z}\ H_1^{(1)}\left(k_\rho|\bar{\rho}-\bar{\rho}'|\right) \quad (2.121)$$

Using the large argument approximation for the Hankel function, the rapidly varying part of the integrand in Eq. 2.121 is asymptotic to the phase factor $e^{ik_\rho|\bar{\rho}-\bar{\rho}'|+ik_{0z}z}$. Thus, the location of the stationary phase point is given by

$$\frac{\partial}{\partial k_\rho}\, i\left(k_\rho|\bar{\rho}-\bar{\rho}'|+k_{0z}z\right)\Big|_{k_{\rho 0}} = 0 \qquad (2.122)$$

The solution is given by

$k_{\rho_0} = k_0 \sin,$

$k_{0z0} = k_0$

cos

(2.123)

with = $\sin^{-1}\frac{|\bar{\rho}-\bar{\rho}'|}{|\bar{r}-\bar{\rho}'|}$, (see Figure2.4).

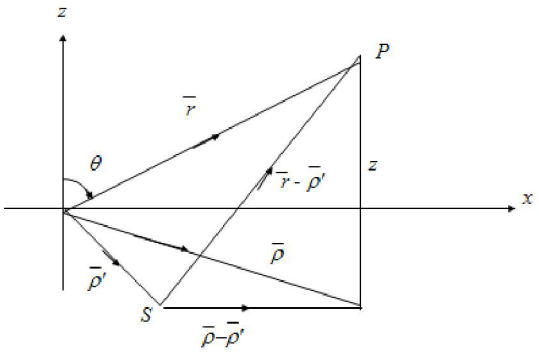

Figure 2.4, Relation between ρ and θ

This leads to the following expression for I_E

$$I_E \sim \frac{-i\; g_E\left(k_{\rho_0}\right) k_{\rho_0}\; e^{-i\pi/2}\; k_{0z0}\; \frac{e^{ik_0|\bar{r}-\bar{\rho}'|}}{|\bar{r}-\bar{\rho}'|}}{}, \quad r \to \infty \qquad (2.124)$$

But

$$|\bar{r}-\bar{\rho}'| \cong r-\hat{r}\cdot\bar{\rho}',$$

thus

$$I_E \sim k_0^2 \sin \quad \cos \quad g_E(k_{\rho_0})\; e^{-i\bar{k}_0\cdot\bar{\rho}'}\; \frac{e^{ik_0 r}}{r}, \; r \to \infty \qquad (2.125)$$

Thus,

$$E_{0z}(\bar{r}) \sim \frac{-i\omega\mu_0}{4\pi}\; k_0^2 \sin \quad \cos \quad \cos \quad g_E(k_{\rho_0})\; \frac{e^{ik_0 r}}{r} \times \iint dx'\, dy'\, J_x(x',y')\; e^{-i\bar{k}_0\cdot\bar{\rho}'} \qquad (2.126)$$

Following similar procedure, getting the magnetic field in the upper half-space as r the following expression

$$H_{0z}(\bar{r}) \sim \frac{i}{4\pi}\; k_0^2 \sin \quad \cos \quad \sin \quad g_H(k_{\rho_0})\; \frac{e^{ik_0 r}}{r} \times \iint dx'\, dy'\, J_x(x',y')\; e^{-i\bar{k}_0\cdot\bar{\rho}'} \qquad (2.127)$$

Thus, using Eq. 2.62 - Eq.2.65, the field patterns are readily obtained.

3. Results

Numerical results of the problem of a microstrip dipole embedded in a substrate-superstrate structure are presented. Numerical computations investigating the effects of the thickness and the anisotropy of the layers on the dipole current distribution and input impedance are performed. Also, the radiation patterns of the microstrip dipole printed in the considered substrate-superstrate structures are calculated.

The numerical computations for the problem under consideration using the dyadic Green's function (DGF) formulation where the moment method (MM) is applied in spectral domain (SD). A microstrip dipole of length $L = 0.5\ \lambda_0$ and width $W = 0.0001\ \lambda_0$, on the top of an isotropic substrate of permittivity $\varepsilon_1 = 3.25\varepsilon_0$ and thickness $h_1 = 0.1016\lambda_0$.

3.1 Printed Dipole on a Single Layer

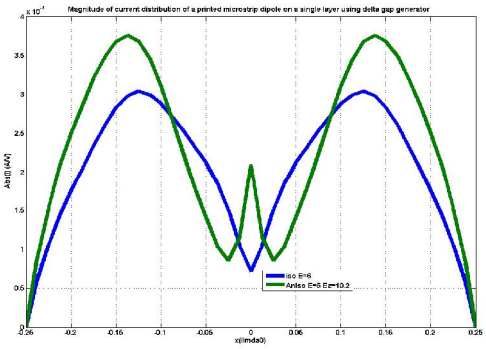

Figure 3.1. Magnitude of current distribution of a printed microstrip dipole on a single layer using delta gap generator with $W/2 = 0.0001l_0$, $L = 0.5\ l_0$, $h = 0.08l_0$.

Figures 3.1show, the magnitude of the current distribution of a printed microstrip dipole on a single layer. The figures indicate that the current distribution undergoes significant changes if the isotropic substrate with $\bar{\bar{\varepsilon}} = 6\varepsilon_0\bar{\bar{I}}$ is substituted by an anisotropic substrate of $\varepsilon = 6\varepsilon_0, \varepsilon_z = 10.2\varepsilon_0$, The magnitude of the current distribution of the dipole on the anisotropic substrate exhibits a rise at the feeding point. Figures 3.2(a) and 3.2(b) show, respectively, the real and imaginary parts of the input impedance. It is clear that the effect of the positive anisotropy

$(\frac{\varepsilon_z}{\varepsilon} > 1)$ of the substrate is to decrease the resonant length relative to the isotropic substrate. Also, the impedance level of the printed dipole on the anisotropic substrate is lower than the dipole on an isotropic substrate. Finally, Figures 3.3(a) and 3.3(b) show, respectively, the E - and H - radiation patterns of the printed dipole. For this considered case, there is no significant differences between the isotropic and anisotropic substrates. However, the H - plane radiation plot shows a slightly lower directivity for the printed dipole on the anisotropic substrate.

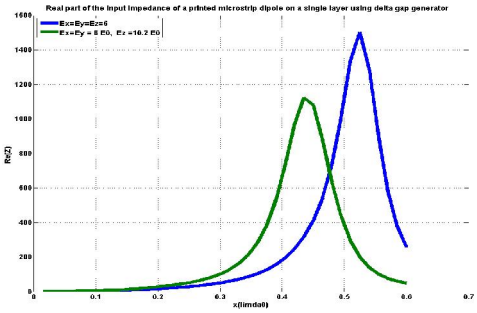

Figure 3.2(a), Real part of the input impedance of a printed microstrip dipole on a single layer using delta gap generator with $W/2 = 0.0001l_0$, $h=0.08l_0$

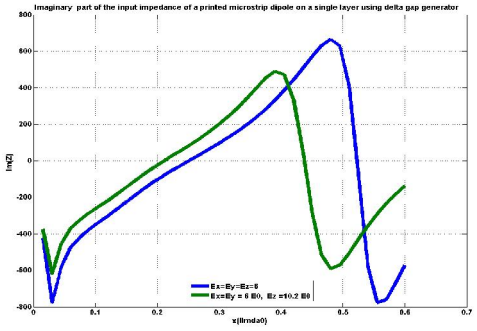

Figure 3.2(b), Imaginary part of the input impedance of a printed microstrip dipole on a single layer using delta gap generator with $W/2 = 0.0001l_0$, $h=0.08l_0$.

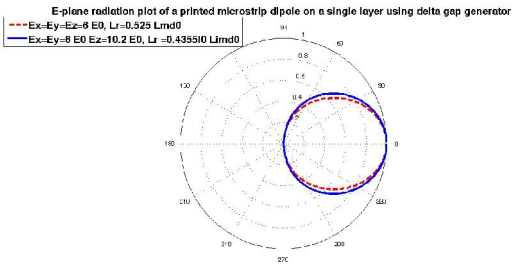

Figure 3.3(a), E-plane radiation plot of a printed microstrip dipole on a single layer using delta gap generator with $W/2 = 0.0001l_0$, $h=0.08l_0$.

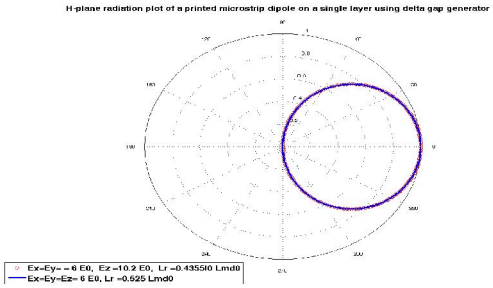

Figure 3.3(b), H-plane radiation plot of a printed microstrip dipole on a single layer using delta gap generator with $W/2 = 0.0001l_0$, $h=0.08l_0$.

3.2 Effect of the superstrate thickness

The effect of the superstrate (cover-layer) thickness is investigated for a printed dipole in a substrate-superstrate configuration. The cover-layer is assumed to be isotropic with permittivity $\bar{\bar{\varepsilon}}_1 = 3.25\varepsilon_0 \bar{\bar{I}}$, $\bar{\bar{\mu}}_1 = \mu_0 \bar{\bar{I}}$ while the substrate is assumed to be uniaxially anisotropic with

$$\bar{\bar{\varepsilon}}_2 = \varepsilon_0 \begin{bmatrix} 6 & 0 & 0 \\ 0 & 6 & 0 \\ 0 & 0 & 10.2 \end{bmatrix}$$

$$\bar{\bar{\mu}}_1 = \mu_0 \bar{\bar{I}}$$

The substrate thickness $h_2 = 0.08\lambda_0$. The dipole of length $L = 0.5\lambda_0$ and width $W = 0.0001\lambda_0$ is fed at the center. The effects of the dielectric cover thickness on the dipole current distribution, input impedance, and radiation patterns are determined. The results are shown in Figures 3.4-3.6, and the following comments are pertinent: 1). The real part of the current distribution, shown in Fig. 3.4(a) is more influenced by the dielectric cover thickness near the center of the dipole. The effect of the thickness of the dielectric cover is negligible when it is increased from $h_1 = 0.05\lambda_0$ to $h_1 = 0.11\lambda_0$. 2). The imaginary part of the current distribution, given in Fig. 3.4(b), also shows some what larger influence of the dielectric cover thickness near the center of the dipole. In addition, it is noted that increasing h_1, the current level is decreased at the center of the dipole. 3). The magnitude of the current distribution, given in Fig. 3.4(c), also shows that the current level is decreased at the center as the thickness of the cover layer increases, however this increase is small in the range of h_1 values considered. The above mentioned effects of the cover dielectric layer were also observed for printed dipoles on isotropic substrates (Newman, 1978). Figures 3.5(a) and 3.5(b) show curves for the real and

imaginary parts of the input impedance at the center of the dipole, respectively, for various values of the dielectric cover thickness h_1. The decrease of the dipole's resonant length for any structure with cover-layer relative to the case with the cover layer thickness $h_1 = 0$ is evident from an inspection of the imaginary part of the input impedance given in Fig. 3.5(b). Also the resonant frequency decreases as the cover thickness increases from $h_1 = 0$ to $h_1 = 0.05\ \lambda_0$, however it increases for values of h_1 larger than $0.05\ \lambda_0$. This effect has also been observed for microstrip dipoles printed in isotropic structures (Uzunoglu *et al.*, 1979). Figures 3.6 show the E- plane radiation patterns for different values of the cover layer thickness.

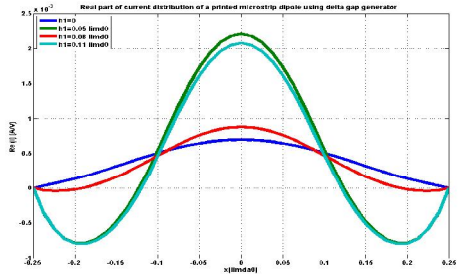

Figure 3.4(a), Real part of current distribution of a printed microstrip dipole using delta gap generator with $W/2 = 0.0001l_0$, $L = 0.5\ l_0$, $h_2 = 0.08l_0$, $e_1 = 3.25\ e_0$, I, $e_2 = 6\ e_0$, $e_{z2} = 10.2\ e_0$

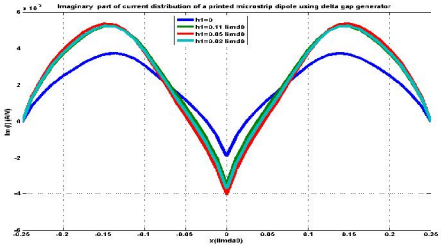

Figure 3.4(b), Imaginary part of current distribution of a printed microstrip dipole using delta gap generator with $W/2 = 0.0001l_0$, $L = 0.5\ l_0$, $h_2 = 0.08l_0$, $e_1 = 3.25$, e_0 I, $e_2 = 6\ e_0$, $e_{z2} = 10.2\ e_0$

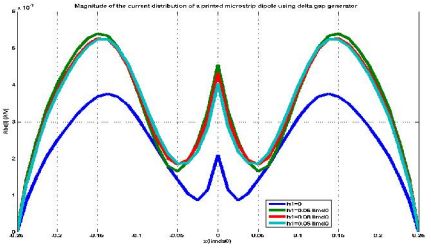

Figure 3.3(c), Magnitude of the current distribution of a printed microstrip dipole using delta gap generator with $W/2 = 0.0001l_0$, $L = 0.5\ l_0$, $h_2 = 0.08l_0$, $e_1 = 3.25\ e_0$ I, $e_2 = 6\ e_0$, $e_{z2} = 10.2\ e_0$

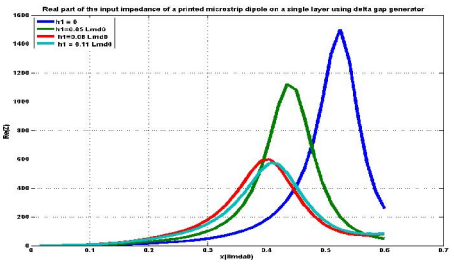

Figure 3.5(a), Real part of the input impedance of a printed microstrip dipole using delta gap generator with $W/2 = 0.0001l_0$, $h_2 = 0.08\ l_0$, $e_1 = 3.25\ e_0$ I, $e_2 = 6\ e_0$, $e_{z2} = 10.2\ e_0$

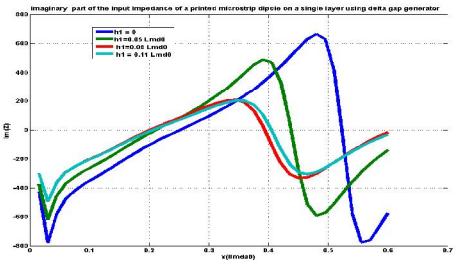

Figure 3.5(b), Imaginary part of the input impedance of a printed microstrip dipole using delta gap generator with $W/2 = 0.0001l_0$, $h_2 = 0.08l_0$, $e_1 = 3.25\ e_0$ I, $e_2 = 6\ e_0$, $e_{z2} = 10.2\ e_0$

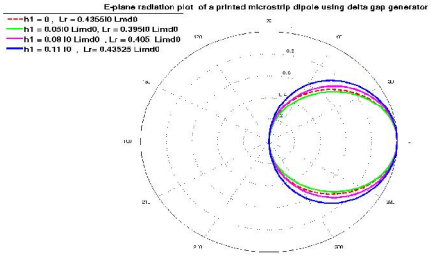

Figure 3.6, E-plane radiation plot of a printed microstrip dipole using delta gap generator with $W/2 = 0.0001l_0$, $h_2 = 0.08\ l_0$, $e_1 = 3.25\ e_0$ I, $e_2 = 6\ e_0$, $e_{z2} = 10.2\ e_0$

3.3 Effect of substrate anisotropy

The effect of substrate anisotropy on the performance of a printed microstrip in substrate-superstrate structure is presented her. The analysis presented in this research is general enough to treat both positive uniaxial ($\varepsilon_z > \varepsilon_x$) and negative uniaxial.

($\varepsilon_z < \varepsilon_x$) cases, as well as wide range of anisotropy ratio

$\frac{\varepsilon_z}{\varepsilon_x}$

(AR =), most substrates in common use are negative uniaxial. As a practical example, is the

Epsilam-10 material having $\varepsilon_x = 13.0\,\varepsilon_0$, $\varepsilon_z = 10.2\,\varepsilon_0$.

Figure. 3.7(a) shows the real part of the dipole's current distribution for a printed dipole on an anisotropic substrate and having isotropic superstrate. Three different substrates are considered; where $\frac{\varepsilon_z}{\varepsilon_x} = \frac{10.2}{6} = 1.7$, $\frac{\varepsilon_z}{\varepsilon_x} = 1$ (isotropic case), and $\frac{\varepsilon_z}{\varepsilon_x} = \frac{10.2}{13} = 0.7846$. The figure shows that the anisotropy ratio has great influence on the real part of the current distribution. Substrates with negative uniaxial material has the largest variation of the real part of the current distribution, while substrates with positive uniaxial material has the smallest variation. Figure 3.7(b) shows that the imaginary part of the dipole's current distribution does not depend too much on the anisotropy ratio. However, the current level is decreased for the case of positive uniaxial material.

Fig. 3.7(c) shows that the magnitude of the dipole's current distribution is the highest for substrates with negative uniaxial material. Figures 3.8(a) and 3.8(b) show the real and imaginary parts, respectively, of the input impedance of the printed microstrip dipole, as function of the electrical length of the dipole for different values of the anisotropy ratios. It is observed that as the anisotropy ratio (AR) decreases, the resonant length of the dipole decreases. Also, the magnitude of the real part of the input impedance decreases with the decrease of the AR. The figures also show that the shift in resonant frequency is about equal to the bandwidth of the microstrip dipole. This implies that a dipole designed for a specific operating frequency may actually resonant outside the dipole bandwidth if the substrate anisotropy is neglected (not considered). Similar conclusion was obtained (Mosig and Gardiol, 1979), for microstrip antennas on single anisotropic substrate. Figures 3.11(a) and 3.11(b) show, respectively, the E- and H- plane radiation patterns for three cases: isotropic substrate with $\varepsilon_2 = \varepsilon_{z2} = 10.2\,\varepsilon_0$, positive uniaxial substrate with $\varepsilon_2 = 6\,\varepsilon_0$, $\varepsilon_{z2} = 10.2\,\varepsilon_0$, and negative uniaxial substrate with $\varepsilon_2 = 13\,\varepsilon_0$, $\varepsilon_{z2} = 10.2\,\varepsilon_0$. In these three cases the superstrate is assumed to be isotropic. The figures show that for the positive uniaxial substrate, the E-plane radiation pattern has higher directivity than the isotropic case while the H- plane radiation pattern has lower directivity. The radiation patterns of the printed circuit dipole on a negative uniaxial substrate exhibits opposite property (E-plane is less directive while the H- plane is more directive than the isotropic case).

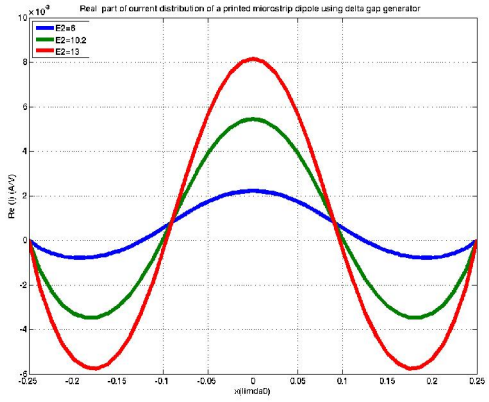

Figure 3.7(a), Real part of current distribution of a printed microstrip dipole using delta gap generator with $W/2 = 0.0001 l_0$, $L = 0.5\ l_0$, $h_1 = h_2 = 0.08\ l_0$, $e_1 = 3.25\ e_0$ I, $e_{z2} = 10.2\ e_0$

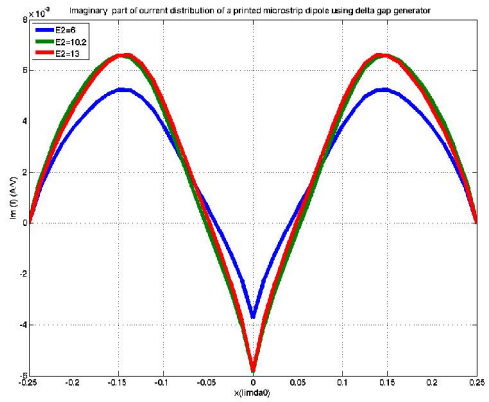

Figure 3.7(b), Imaginary part of current distribution of a printed microstrip dipole using delta gap generator with $W/2 = 0.0001 l_0$, $L = 0.5\ l_0$, $h_1 = h_2 = 0.08\ l_0$, $e_1 = 3.25\ e_0$ I, $e_{z2} = 10.2\ e_0$

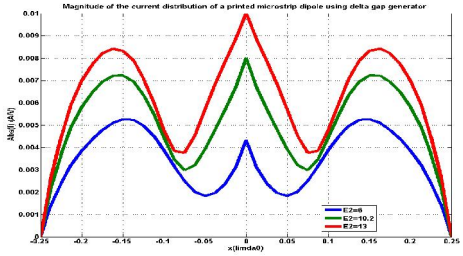

Figure 3.7(c), Magnitude of the current distribution of a printed microstrip dipole using delta gap generator with $W/2 = 0.0001 l_0$, $L = 0.5\ l_0$, $h_1 = h_2 = 008\ l_0$, $e_1 = 3.25\ e_0$ I, $e_{z2} = 10.2\ e_0$

3.4 Effect of cover-layer anisotropy

Figures. 3.10(a)- 3.10(c) show, respectively, the real part, imaginary part, and the magnitude of the current distribution of a printed dipole in a two-layer

microstrip structure having isotropic substrate and anisotropic superstrate. It is observed that the behavior of the current distribution is almost the same as the previous case where the substrate is anisotropic with isotropic cover-layer. However, the variation of the imaginary part of the current distribution is more pronounced (Figures 3.11(a) and3.11(b) show, respectively, the real and imaginary parts of the dipole's input impedance. The data show similar behavior to that observed in the previous case. Here, it is also observed that the resonant length of the dipole decreases with decrease of the anisotropy ratio. Figures 3.12(a) and 3.12(b) show, respectively, the E- and H- plane radiation patterns as function of the AR of the superstrate where the substrate is isotropic dipole. Observe the singularly in the dipole current at the probe location. Figure 3.14 shows the real and imaginary parts of the input impedance. Since the problem is formulated using an idealized probe feed which does not account to the probe self reactance, a self inductive reactance term $X_p = 60\, k_0\, h_2\, \ln(k_2^e\, R)$ is added to the result as a correction factor (Dernerydm, 1977). Finally, Figure 3.15 shows the radiation pattern for this case.

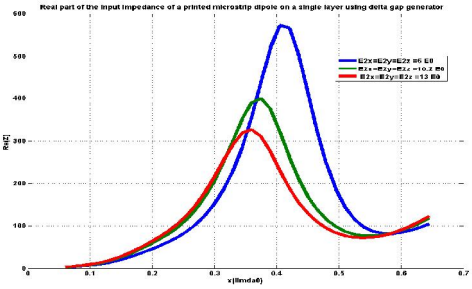

Figure 3.8(a), Real part of the input impedance of a printed microstrip dipole using delta gap generator with $W/2 = 0.0001 l_0$, $h_1 = h_2 = 0.08\ l_0$, e_1 =3.25 e_0 I, $e_{z2} = 10.2\ e_0$

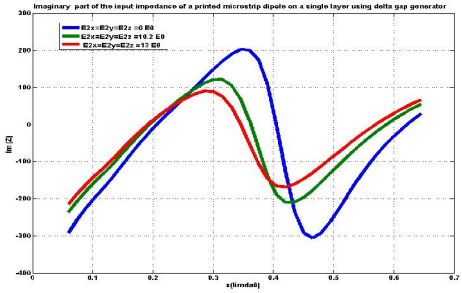

Figure 3.8(b), Imaginary part of the input impedance of a printed microstrip dipole using delta gap generator with $W/2 = 0.0001 l_0$, $h_1 = h_2 = 0.08\ l_0$, e_1 =3.25 e_0 I, $e_{z2} = 10.2\ e_0$

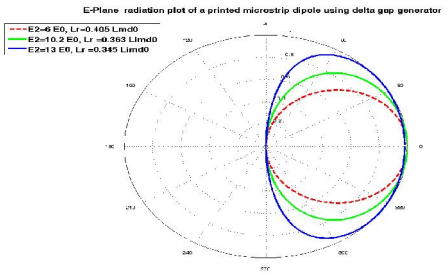

Figure 3.9(a), E-Plane radiation plot of a printed microstrip dipole using delta gap generator with $W/2 = 0.0001 l_0$, $h_1 = h_2 = 0.08 l_0$, e_1 =3.25 e_0 I, $e_{z2} = 10.2\ e_0$

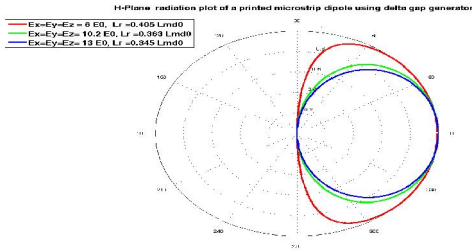

Figure 3.9(b), H-Plane radiation plot of a printed microstrip dipole using delta gap generator with $W/2 = 0.0001 l_0$, $h_1 = h_2 = 0.08 l_0$, e_1 =3.25 e_0 I, $e_{z2} = 10.2\ e_0$

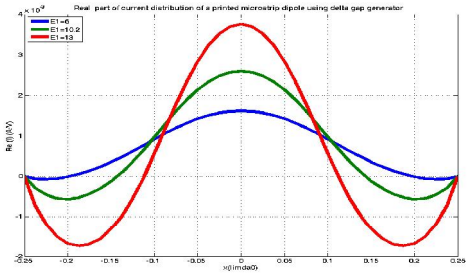

Figure 3.10(a), Real part of current distribution of a printed microstrip dipole using delta gap generator with $W/2 = 0.0001 l_0$, L= 0.5 l_0, $h_1 = h_2 = 0.08 l_0$, e_2 =3.25 e_0 I, $e_{z1} = 10.2\ e_0$

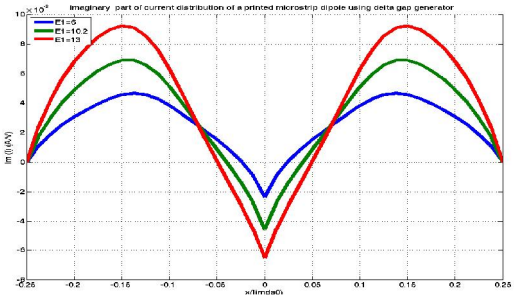

Figure 3.10(b), Imaginary part of current distribution of a printed microstrip dipole using delta gap generator with $W/2 = 0.0001 l_0$, L= 0.5 l_0, $h_1 = h_2 = 0.08 l_0$, e_2 =3.25 e_0 I, $e_{z1} = 10.2\ e_0$

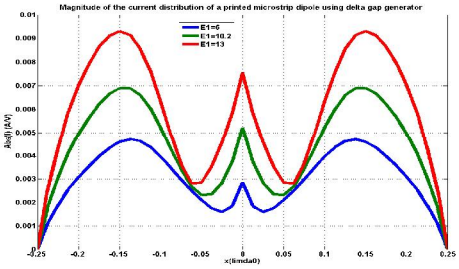

Figure 3.10(c), Magnitude of the current distribution of a printed microstrip dipole using delta gap generator with $W/2 = 0.0001l_0$, $L= 0.5\ l_0$, $h_1 = h_2 = 0.08l_0$, $e_2 =3.25\ e_0$ $I,\ e_{z1} = 10.2\ e_0$

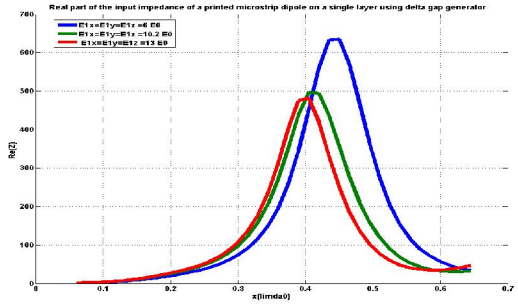

Figure 3.11(a), Real part of input impedance of a printed microstrip dipole using delta gap generator with $W/2 = 0.0001l_0$, $h_1 = h_2 = 0.08\ l_0$, $e_2 =3.25\ e_0$ $I,\ e_{z1} = 10.2\ e_0$

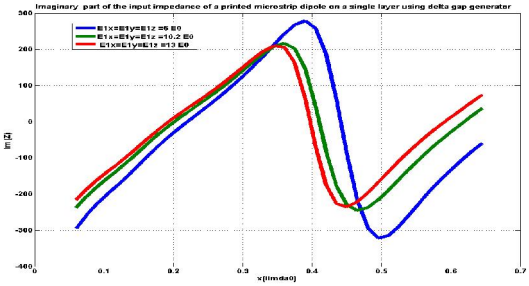

Figure 3.11(b), Imaginary part of input impedance of a printed microstrip dipole using delta gap generator with $W/2 = 0.0001l_0$, $h_1 = h_2 = 0.08\ l_0$, $e_2 =3.25\ e_0$ $I,\ e_{z1} = 10.2\ e_0$

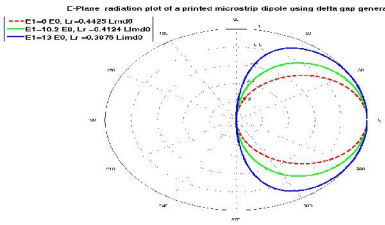

Figure 6.12(a), E-Plane radiation plot of a printed microstrip dipole using delta gap model with $W/2 = 0.0001l_0$, $h_1 = h_2 = 0.08\ l_0$, $e_2 =3.25\ e_0$ $I,\ e_{z1} = 10.2\ e_0$

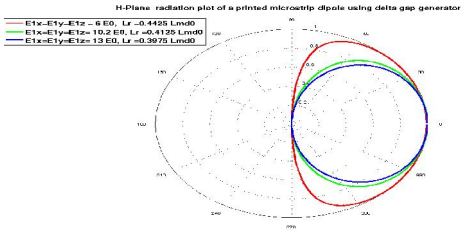

Figure 6.12(b), H-Plane radiation plot of a printed microstrip dipole using delta gap model with $W/2 = 0.0001l_0$, $h_1 = h_2 = 0.08\ l_0$, $e_2 =3.25\ e_0$ $I,\ e_{z1} = 10.2\ e_0$

3.5 Probe-fed printed circuit dipole

Figure 3.13 shows the real and imaginary part of the current distribution of a probe-fed microstrip

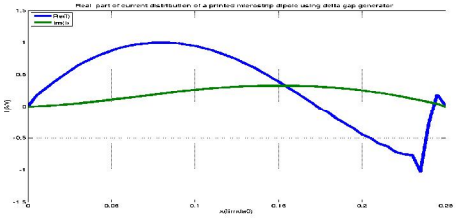

Figure 3.13. Current distribution of a printed microstrip dipole for probe excitation with radius $R=0.0004l_0$, $W/2 = 0.0008l_0$, $L=0.25\ l_0$, $h_1 = h_2 =0.08l_0$, $e_1 =3.25\ e_0$, $I,\ e_2 = 13\ e_0$, $e_{z1} = 10.2\ e_0$, $x_0 =0.239833l_0$

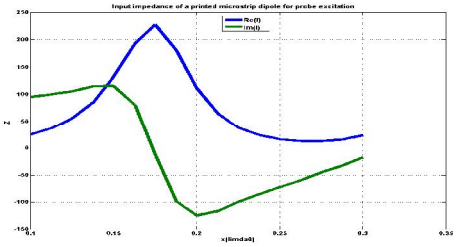

Figure 3.14, Input impedance of a printed microstrip dipole for probe excitation with radius $R=0.0004l_0$, $W/2 = 0.0008l_0$, $h_1 = h_2 = 0.08l_0$, $e_1 =3.25\ e_0$ $I,\ e_2 = 13\ e_0$, $e_{z1} = 10.2\ e_0$, $x_0 =0.239833l_0$

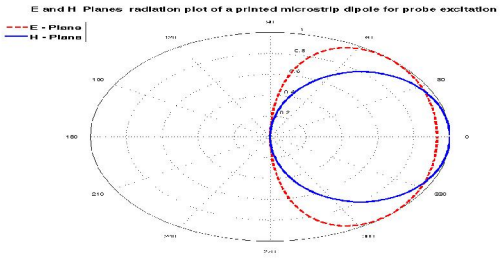

Figure 3.15, E and H Planes radiation plot of a printed microstrip dipole for probe excitation with

R=0.0004l_0 W/2 = 0.0008l_0, $h_1 = h_2$ = 0.08 l_0, L_r = 0.175 l_0, e_1 =3.25 e_0 I, e_2 =13e_0, e_{z2} = 10.2 e_0, x_0 = 0.239833l_0

3.6 Farfield Directivities of one Printed Dipole on Two-Layer Substrates

A two-layer Substrates for a printed dipole with an anisotropic substrate was considered now. The printed dipole was placed two in layers substrates, with thickness were set $h_1 = 01016\,\lambda_0$ and $h_2 = 0.08\,\lambda_0$.(See Table 1).

Table 1. Farfield Directivities of Printed microstrip patches placed in different Layers.

	Phi Gain dBi	Phi in degree	Theta Gain dBi	Theta in degree
1 Layer 1 dipole (2.3)	2.3	90	4.9	81
2 Layer 1 dipole (2.3)	0.6	30	1.8	102
2 Layer 1 dipole (6,6,10.2)	4.7	0	4.3	294
2 Layer 1 dipole (10.2,10.2,10.2)	4.8	0	1.4	196.7
2 Layer 1 dipole (13,13,10.2)	4.7	40	6.9	233
2 Layer 2 dipole (2.3)	0.8	4	5.1	252
2 Layer 2 dipole (6,6,10.2)	5.7	0	4.1	250
2 Layer 2 dipole (10.2,10.2,10.2)	5.2	0	1	259
2 Layer 2 dipole (13,13,10.2)	4.7	37	6.6	306

3.6.1 For isotropic case

Where $\varepsilon_x = \varepsilon_y = \varepsilon_z = 2.3\,\varepsilon_0$. The main lobe magnitude for Phi =90 was 0.6 dB with 30 degree main lobe direction. But the main lobe magnitude for Theta =90 was 1.8 dB with 102 degree in main lobe direction.

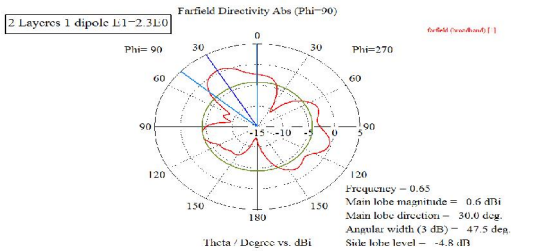

Figure 3.16, Farfield Directivity (φ = 90°) of Patch placed on the top of a isotropic substrate (2 Layers – 1 Patch) with Length L = 0.6 λ_0, Width W=0.0004 λ_0, Substrate Thickness h_1= 0.1016 λ_0 and ε_1 =2.3 ε_0

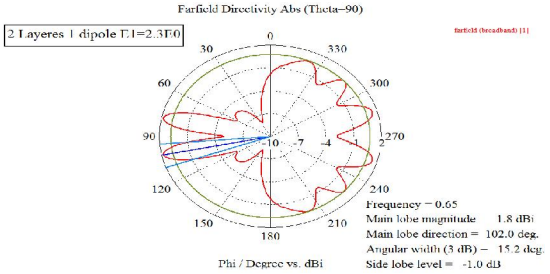

Figure 3.17, Farfield Directivity (ɵ = 90°) of Patch placed on the top of a isotropic substrate (2 Layers – 1 Patch) with Length L = 0.6 λ_0, Width W=0.0004 λ_0, Substrate Thickness h_1= 0.1016 λ_0 and ε_1 =2.3 ε_0

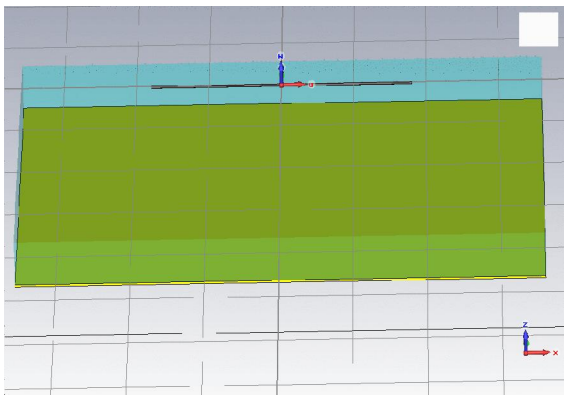

Figure 3.18, Printed microstrip patch placed on the top of a isotropic substrate (2 Layers – 1 Patch) with patch Length L = 0.6 λ_0, Width W=0.0004 λ_0, Substrate Thickness h_1= 0.1016 λ_0 and ε_1 =2.3 ε_0

3.6.2 For anisotropic case

Where $\varepsilon_1 = \varepsilon_{iz} = 6\,\varepsilon_0$ *and* $\varepsilon_2 = 10.2\,\varepsilon_0$. The main lobe magnitude for Phi =90 was 4.7 dB with 0 degree main lobe direction. But the main lobe magnitude for Theta =90 was 4.3 dB with 294 degree in main lobe direction.

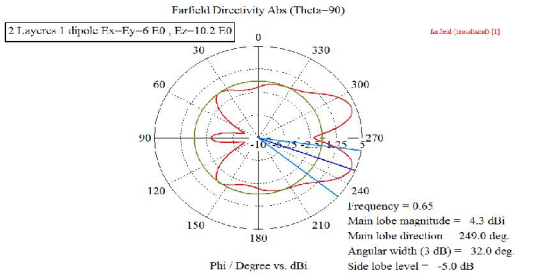

Figure 3.19, Farfield Directivity (ɵ = 90°) of Patch placed on the top of an anisotropic substrate (2 Layers – One Patch) with Length L = 0.6 λ_0, Width W=0.0004 λ_0, Substrate Thickness $h_1$0.1016 λ_0 and ε_1 =3.25 ε_0, $\varepsilon_x = \varepsilon_y = 6\,\varepsilon_0$, ε_z= 10.2 ε_0

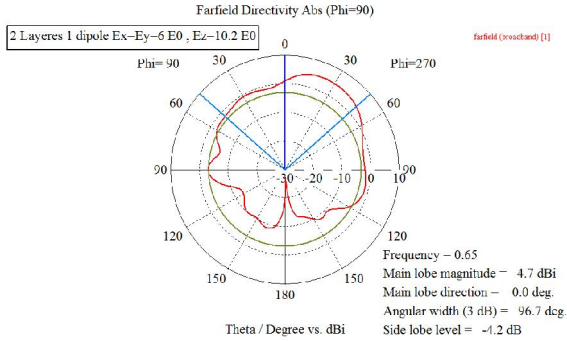

Figure 3.20, Farfield Directivity (φ = 90°) of Patch placed on the top of a anisotropic substrate (2 Layers – 1 Patch) with Length L = 0.6 λ_0, Width W=0.0004 λ_0, Substrate Thickness h_1= 0.1016 λ_0 and ε_1 =3.25 ε_0, $\varepsilon_x = \varepsilon_y = 6\,\varepsilon_0$, ε_z= 10.2 ε_0

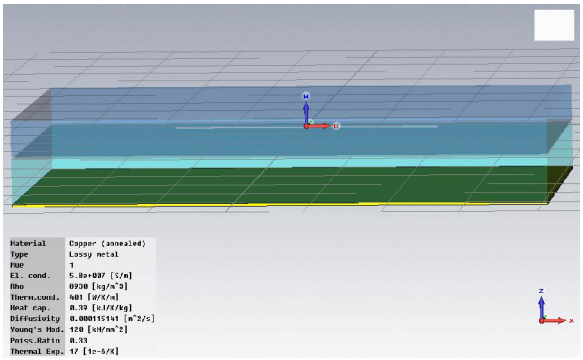

Figure 3.21, Printed microstrip patch placed on the top of a isotropic substrate (2 Layers – 1 Patch) with patch Length L = 0.6 λ_0, Width W=0.0004 λ_0, Substrate Thickness h_1= 0.1016 λ_0 and ε_1 =3.25 ε_0, $\varepsilon_x = \varepsilon_y$ = 6 ε_0, ε_z= 10.2 ε_0

3.6.3 For isotropic case

Where $\varepsilon_1 = \varepsilon_{iz} = \varepsilon_2 = 10.2\,\varepsilon_0$. The main lobe magnitude for Phi =90 was 4.8 dB with 0 degree main lobe direction. But the main lobe magnitude for Theta =90 was 1.4 dB with 196.7 degree in main lobe direction.

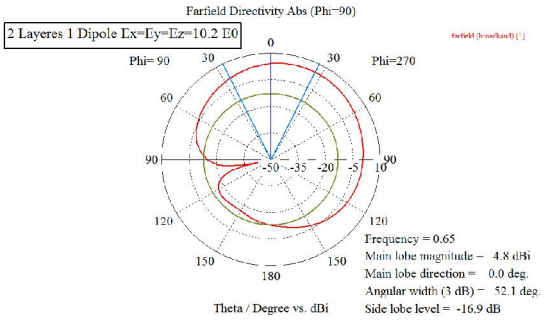

Figure 3.22, Farfield Directivity (φ = 90°) of Patch placed on the top of a isotropic substrate (2 Layers – 1 Patch) with Length L = 0.6 λ_0, Width W=0.0004 λ_0, Substrate Thickness h_1= 0.1016 λ_0 and ε_1 =10.2 ε_0

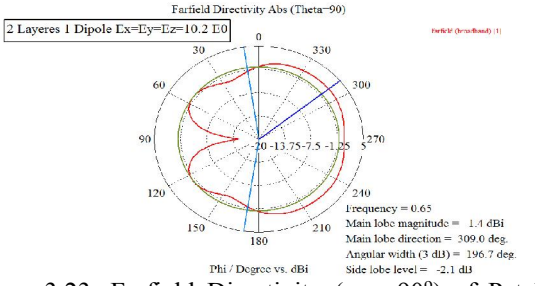

Figure 3.23, Farfield Directivity (ɵ = 90°) of Patch placed on the top of a isotropic substrate (2 Layers – 1 Patch) with Length L = 0.6 λ_0, Width W=0.0004 λ_0, Substrate Thickness h_1= 0.1016 λ_0 and ε_1 =10.2 ε_0

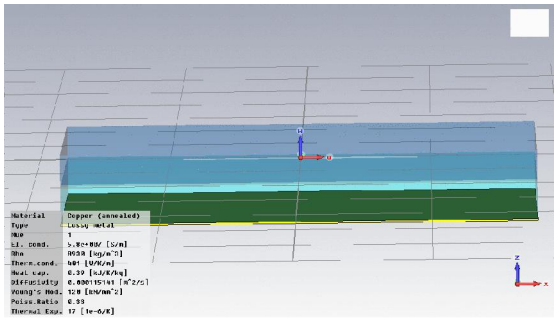

Figure 3.24, Printed microstrip patch placed on the top of a isotropic substrate (2 Layers – 1 Patch) with patch Length L = 0.6 λ_0,Width W=0.0004 λ_0, Substrate Thickness h_1= 0.1016 λ_0 and ε_1 =3.25 ε_0

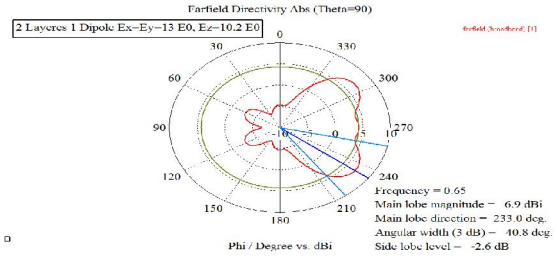

Figure 3.25, Farfield Directivity (ɵ = 90°) of Patch placed on the top of a isotropic substrate (2 Layers – 1 Patch) with Length L = 0.6 λ_0, Width W=0.0004 λ_0, Substrate Thickness h_1= 0.1016 λ_0 and ε_1 =3.25 ε_0, $\varepsilon_x = \varepsilon_y$ = 13 ε_0, ε_z= 10.2 ε_0

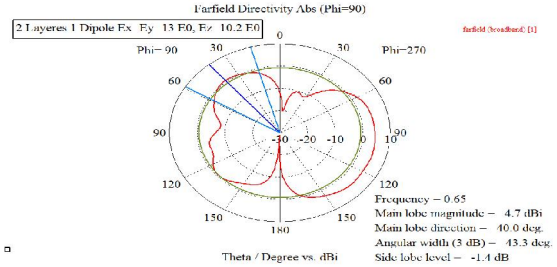

Figure 3.26, Farfield Directivity (φ = 90°) of Patch placed on the top of a isotropic substrate (2 Layers – 1 Patch) with Length L = 0.6 λ_0, Width W=0.0004 λ_0, Substrate Thickness h_1= 0.1016 λ_0 and ε_1 =3.25 ε_0, $\varepsilon_x = \varepsilon_y$ = 13 ε_0, ε_z= 10.2 ε_0

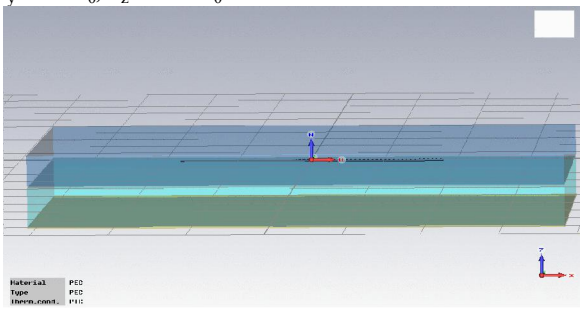

Figure 3.27, Printed microstrip patch placed on the top of a isotropic substrate (2 Layers – 1 Patch) with patch Length L = 0.6 λ_0,Width W=0.0004 λ_0, Substrate Thickness h_1= 0.1016 λ_0 and ε_1 =3.25 ε_0

3.6.4 For anisotropic case

Where $\varepsilon_1 = \varepsilon_{iz} = 13\,\varepsilon_0$ *and* $\varepsilon_2 = 10.2\,\varepsilon_0$. The main lobe magnitude for Phi =90 was 4.7 dB with 40 degree main lobe direction. But the main lobe magnitude for Theta =90 was 6.9 dB with 233 degree in main lobe direction.

3.7 Farfield Directivities of Two Printed Dipoles on Two-Layer Substrates

A two-layer Substrats for Two printed dipoles with an anisotropic superstrate was considered nest. The printed dipole in Fig. 1 was placed two layers substrats, with thickness were set $h_1 = 01016\,\lambda_0$ and $h_2 = 0.08\,\lambda_0$. See Table 1.

3.7.1 For isotropic case

Where $\varepsilon_1 = \varepsilon_2 = 2.3\,\varepsilon_0$. The main lobe magnitude for Phi =90 was 0.8 dB with 4 degree main lobe direction. But the main lobe magnitude for Theta =90 was 5.1 dB with 252 degree in main lobe direction.

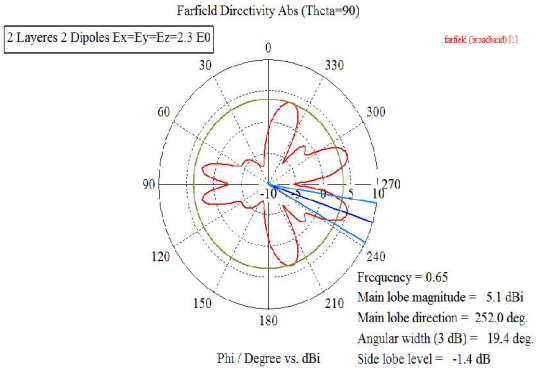

Figure 3.28, Farfield Directivity (ɵ = 90°) of Patch placed on the top of a isotropic substrate (2 Layers – 2 Patches) with Length L = 0.6 λ_0, Width W=0.0004 λ_0, Substrate Thickness h_1= 0.1016 λ_0 and ε_1 =2.3 ε_0

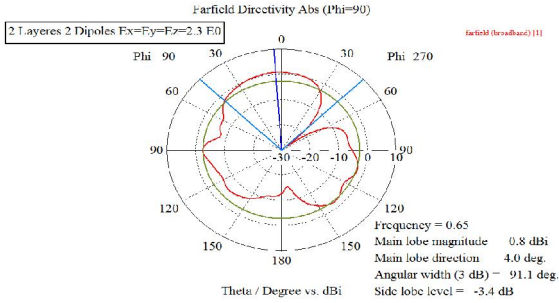

Figure 3.29, Farfield Directivity (φ = 90°) of Patch placed on the top of a isotropic substrate (2 Layers – 2 Patches) with Length L = 0.6 λ_0, Width W=0.0004 λ_0, Substrate Thickness h_1= 0.1016 λ_0 and ε_1 =2.3 ε_0

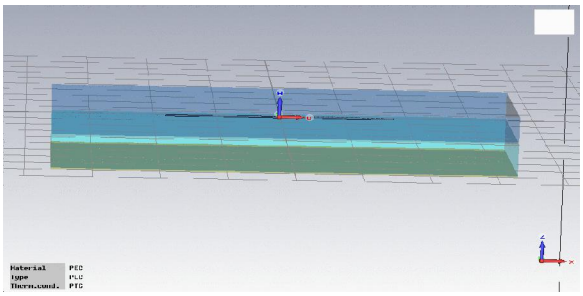

Figure 3.30, Printed microstrip patch placed on the top of a isotropic substrate (2 Layers – 2 Patches) with patch Length L = 0.6 λ_0,Width W=0.0004 λ_0, Substrate Thickness h_1= 0.1016 λ_0 and ε_1 =2.3 ε_0

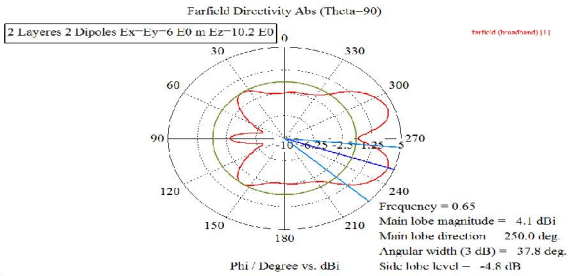

Figure 3.31, Farfield Directivity (ɵ = 90°) of Patch placed on the top of a isotropic substrate (2 Layers – 2 Patches) with Length L = 0.6 λ_0, Width W=0.0004 λ_0, Substrate Thickness h_1= 0.1016 λ_0 and ε_1 =3.25 ε0, εx = εy = 6 ε0, εz= 10.2 ε0

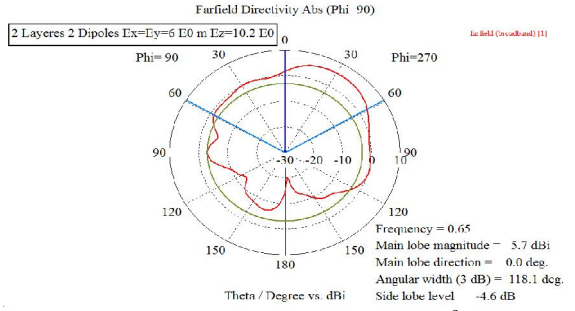

Figure 3.32, Farfield Directivity (φ = 90°) of Patch placed on the top of a isotropic substrate (2 Layers – 2 Patches) with Length L = 0.6 λ_0, Width W=0.0004 λ_0, Substrate Thickness h_1= 0.1016 λ_0 and ε1 =3.25 ε0, εx = εy = 6 ε_0, εz= 10.2 ε_0

3.7.2 For anisotropic case

Where $\varepsilon_1 = \varepsilon_{iz} = 6\,\varepsilon_0$ *and* $\varepsilon_2 = 10.2\,\varepsilon_0$. The main lobe magnitude for Phi =90 was 5.7 dB with 0 degree main lobe direction. But the main lobe magnitude for Theta =90 was 4.1 dB with 250 degree in main lobe direction.

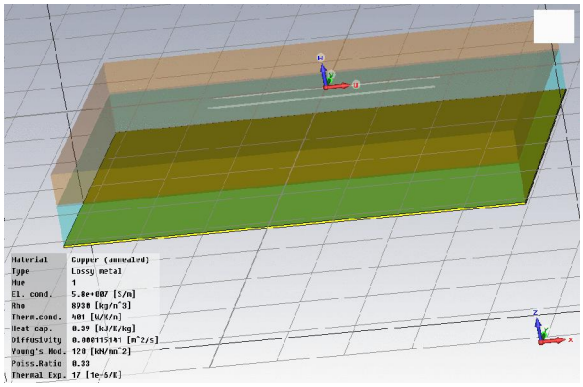

Figure 3.33, Printed microstrip patch placed on the top of a anisotropic substrate (2 Layers – 2 Patches) with patch Length L = 0.6 λ_0,Width W=0.0004 λ_0, Substrate Thickness $h_{1=}$ 0.1016 λ_0 and ε_1 =3.25 ε_0, ε_x = ε_y = 6 ε_0, ε_z= 10.2 ε_0

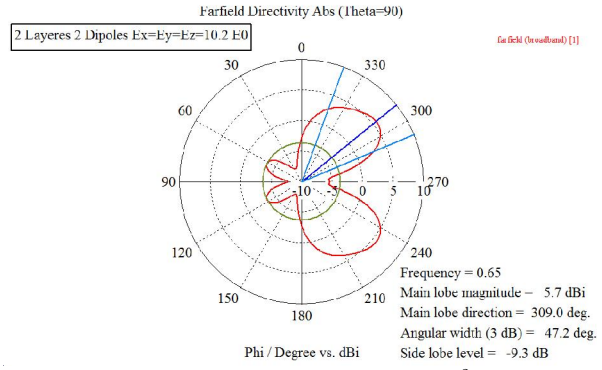

Figure 3.34, Farfield Directivity (ɵ = 90°) of Patch placed on the top of a isotropic substrate (2 Layers – 2 Patches) with Length L = 0.6 λ_0, Width W=0.0004 λ_0, Substrate Thickness $h_{1=}$ 0.1016 λ_0 and ε_1 =10.2 ε_0

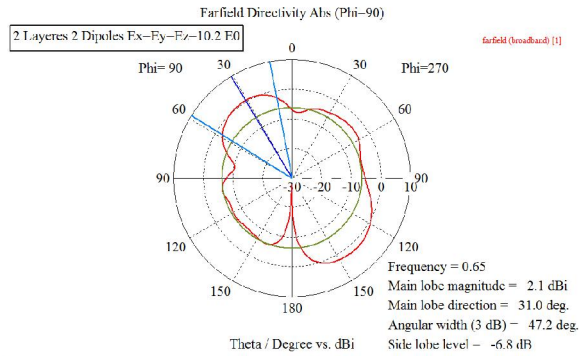

Figure 3.35, Farfield Directivity (φ = 90°) of Patch placed on the top of a isotropic substrate (2 Layers – 2 Patches) with Length L = 0.6 λ_0, Width W=0.0004 λ_0, Substrate Thickness $h_{1=}$ 0.1016 λ_0 and ε_1 =10.2 ε_0

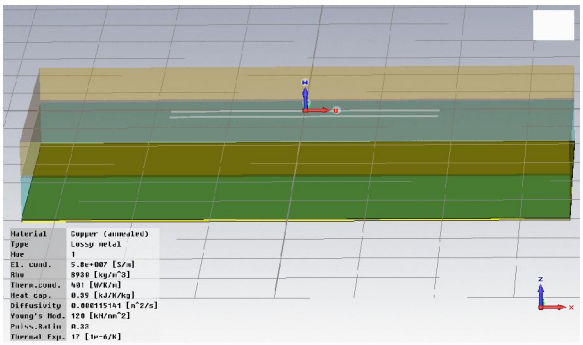

Figure 3.36, Printed microstrip patch placed on the top of a isotropic substrate (2 Layers – 2 Patches) with patch Length L = 0.6 λ_0,Width W=0.0004 λ_0, Substrate Thickness $h_{1=}$ 0.1016 λ_0 and ε_1 =10.2 ε_0

3.7.3 For anisotropic case

Where $\varepsilon_1 = \varepsilon_{iz} = \varepsilon_2 = 10.2\ \varepsilon_0$. The main lobe magnitude for Phi =90 was 5.2 dB with 0 degree main lobe direction. But the main lobe magnitude for Theta =90 was 1 dB with 259 degree in main lobe direction.

3.7.4 For anisotropic case

Where $\varepsilon_1 = \varepsilon_{iz} = 13\ \varepsilon_0\ and\ \varepsilon_2 = 10.2\ \varepsilon_0$. The main lobe magnitude for Phi =90 was 4.7 dB with 37 degree main lobe direction. But the main lobe magnitude for Theta =90 was 6.6 dB with 306 degree in main lobe direction

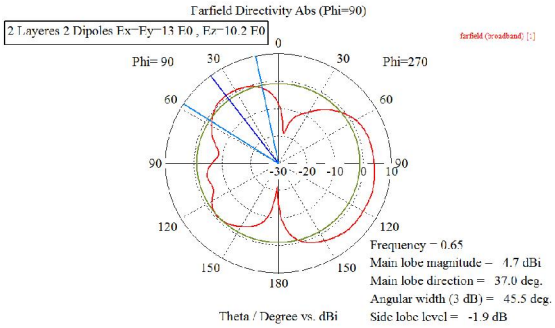

Figure 3.37, Farfield Directivity (φ = 90°) of Patch placed on the top of a isotropic substrate (2 Layers – 2 Patch) with Length L = 0.6 λ_0, Width W=0.0004 λ_0, Substrate Thickness $h_{1=}$ 0.1016 λ_0 and ε_1 =3.25 ε_0, ε_x = ε_y = 13 ε_0, ε_z= 10.2 ε_0

3.8 Single-Element Antenna Design and Improved Single-Element Antenna Design by using anisotropic layer

The design parameters for the antenna are detailed below:

- L= 10.40 mm(Antenna length)
- W= 25.4 mm (Antenna Width)
- H= 1.48 mm (Substrate Height)
- ϵ_r= 4.3 (Permittivity of FR4)
- Mt=.038 mm (Metal Thickness)

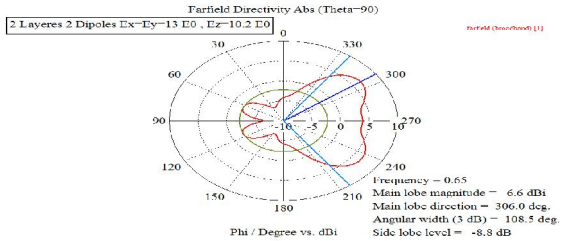

Figure 3.38, Farfield Directivity (ɵ = 90°) of Patch placed on the top of a isotropic substrate (2 Layers – 2 Patches) with Length L = 0.6 λ_0, Width W=0.0004 λ_0, Substrate Thickness h_1= 0.1016 λ_0 and ε_1 =3.25 ε_0, ε_x = ε_y = 13 ε_0, ε_z= 10.2 ε_0

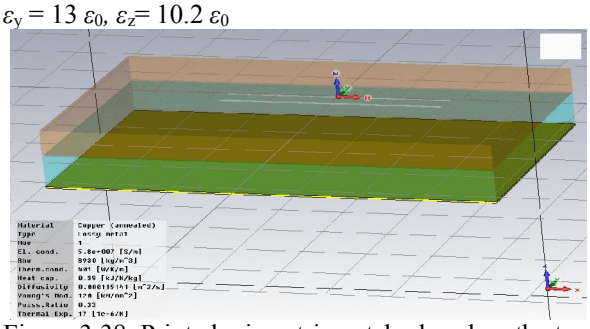

Figure 3.38, Printed microstrip patch placed on the top of a isotropic substrate (2 Layers – 2 Patches) with patch Length L = 0.6 λ_0,Width W=0.0004 λ_0, Substrate Thickness h_1= 0.1016 λ_0 and ε_1 =3.25 ε_0, ε_x = ε_y = 13 ε_0, ε_z= 10.2 ε_0

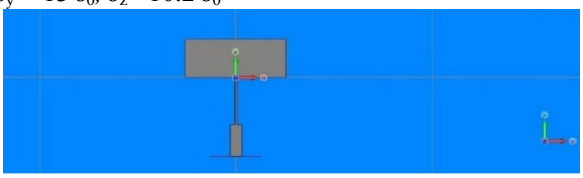

Figure 3.39 The patch antenna

The farfield realized gain plots is within acceptable range to deem the antenna an effective and efficient radiator in the ISM band.

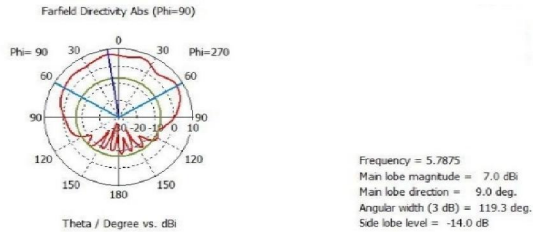

Figure 3.40. Farfield realized gain plot for patch antenna

The Improved design (1) parameters for the antenna are detailed below:

For layer 1

- L1= 10.40 mm(Antenna length)
- W1= 25.4 mm (Antenna Width)
- H1= 1.48 mm (Substrate Height)
- $\in_{r(x,y,z)}$= (6,6,10.2)
- Mt=.038 mm (Metal Thickness)

For layer 2

- L2= 10.40 mm(Antenna length)
- W2= 25.4 mm (Antenna Width)
- H2= 1.48 mm (Substrate Height)
- $\in_{r(x,y,z)}$= (6,6,10.2)
- Mt=.038 mm (Metal Thickness)

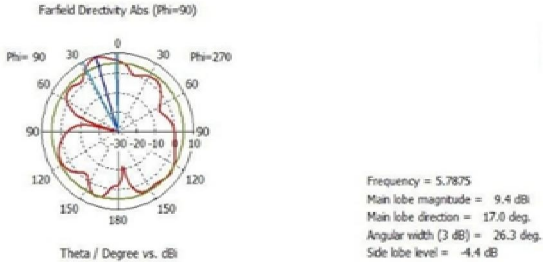

Figure 3.41 Farfield realized gain plot for patch antenna ($\in_{r(x,y,z)}$= (6,6,10.2))

The Improved design (2) parameters for the antenna are detailed below:

For layer 1

- L1= 10.40 mm(Antenna length)
- W1= 25.4 mm (Antenna Width)
- H1= 1.48 mm (Substrate Height)
- $\in_{r(x,y,z)}$= (10.2,10.2,10.2)
- Mt=.038 mm (Metal Thickness)

For layer 2

- L2= 10.40 mm(Antenna length)
- W2= 25.4 mm (Antenna Width)
- H2= 1.48 mm (Substrate Height)
- $\in_{r(x,y,z)}$= (10.2,10.2,10.2)
- Mt=.038 mm (Metal Thickness)

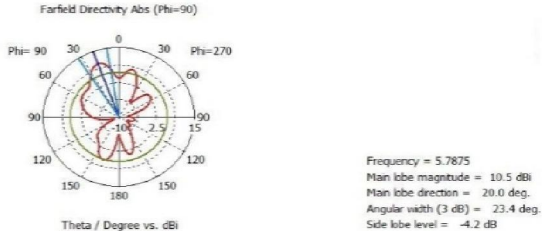

Figure 3.42 Farfield realized gain plot for patch antenna ($\in_{r(x,y,z)}$= (10.2,10.2,10.2))

The Improved design (3) parameters for the antenna are detailed below:

For layer 1

- L1= 10.40 mm(Antenna length)
- W1= 25.4 mm (Antenna Width)
- H1= 1.48 mm (Substrate Height)
- $\in_{r(x,y,z)}$= (13,13,10.2)
- Mt=.038 mm (Metal Thickness)

For layer 2

- L2= 10.40 mm(Antenna length)

- W2= 25.4 mm (Antenna Width)
- H2= 1.48 mm (Substrate Height)
- $\epsilon_{r(x,y,z)}$= (13,13,10.2)
- Mt=.038 mm (Metal Thickness)

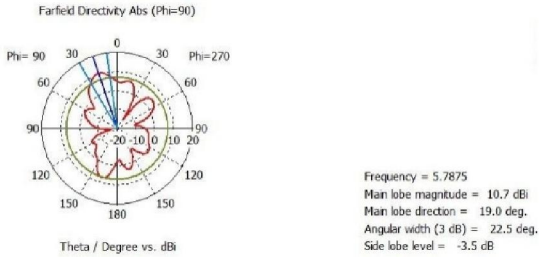

Figure 3.43 Farfield realized gain plot for patch antenna ($\epsilon_{r(x,y,z)}$= (13,13,10.2))

The Improved design (4) parameters for the antenna are detailed below:

For layer 1

- L1= 10.40 mm(Antenna length)
- W1= 25.4 mm (Antenna Width)
- H1= 1.48 mm (Substrate Height)
- $\epsilon_{r(x,y,z)}$= (13,13,10.2)
- Mt=.038 mm (Metal Thickness)

For layer 2

- L2= 10.40 mm(Antenna length)
- W2= 25.4 mm (Antenna Width)
- H2= 1.48 mm (Substrate Height)
- $\epsilon_{r(x,y,z)}$= (18,18,10.2)
- Mt=.038 mm (Metal Thickness)

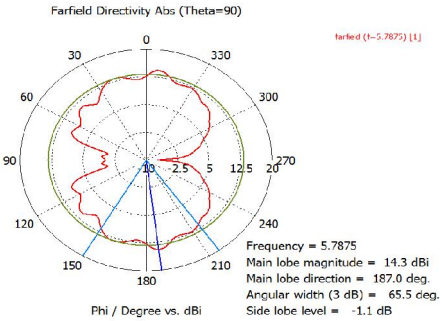

Figure 4.28 Farfield realized gain plot for patch antenna ($\epsilon_{r(x,y,z)}$= (18,18,10.2))

Acknowledgements:

Authors are grateful to Mr. Mubsher for all support to carry out this work.

Corresponding Author:
Mamdoh Gharbi

Department of Electrical and Computer Engineering, King Abdul Aziz University
P O Box: 80204, Jeddah 21589
E-mail: mamdohgharbi@yahoo.com

4/8/2015

References

1. Abramowitz M. and I. A. Stegun," Handbook of Mathematical Functions," New York: Wiley Interscience, 1986.
2. Byron E. V.," A New Flush-Mounted Antenna Element for Phased Array Application," in Proc. Phased Array Antennas Symposium, pp. 187-192, 1970.
3. Carver K. R.," A Model Expansion Theory for The Microstrip Antenna," Dig. Int. Sump. Antenna Propagation Soc., Seattle, WA. pp. 101-104 June 1979.
4. Carver K. R. and J. W. Mink," Microstrip Antenna Technology," IEEE Trans. on Antennas and Propagation, Vol. AP-29a, NO. 1, pp 2-24, January 1981.
5. Derneryd A. G.," A Theoretical Investigation of the Rectangular Microstrip Antenna Element," Rome Air Development Center, Tech. Rpt.TR-77-206, June 1977.
6. Deschamps G. A., "Microstrip Microwave Antennas." presented at 3rd USAF Symposium on Antennas, 1953.
7. Gurel C. S. and E. Yazgan., "Characteristics of a circular patch microstrip antenna on uniaxially anisotropic substrate," *IEEE Trans. Antennas Propag.*, vol. 52, no.. 10, pp. 2532–2537, Oct. 2004.
8. Gutton H. and G. Baissinot, "Flat Aerial for Ultra High Frequencies," French Patent No. 703113, 1955.
9. Lo Y. T., D. D. Harrison, D. Solomon, G. A. Deschamps and F. R. Ore," Study of Microstrip Antennas, Microstrip Phased Arrays, and Microstrip Feed Networks," Rome Air Development Center, Tech Rpt. TR-77-406, October 1977.
10. Lo Y. T., D. Solomon and W. F. Richards," Theory and Experiment on Microstip Antennas, " IEEE Trans. on Antennas and Propagation, Vol. AP-27, No. 2, pp. 137-145, March 1979.
11. Mosig J. R. and F. E Gardiol," The Near Field of An Open Microstrip Structure," IEEE AP – S International Symposium, pp. 379 - 382, 1979.
12. Munson R. E.," Conformal Microstrip Antennas and Microstrip Phased Arrays," IEEE Trans. on Antennas and Propagation, Vol. AP-22. No. 1, pp. 74-78, January 1974.
13. Newman E. H. and P. Tulyathan," Analysis of Microstrip Antennas using Moment Methods," IEEE Trans, on Antennas and Propagation," Vol. AP- 29, No. 1, pp. 47-53, January 1981.
14. Newman E. H.," Strip Antennas in a Dielectric Slab," IEEE Trans. on Antennas and Propagation, Vol. AP-26, No. 5, pp 647-653, September 28, 1978.
15. Pozar D. M., " Considerations for Millimeter Wave printed Antennas," IEEE Trans. on Antennas and Propagation, Vol. AP-31, No. 5. pp. 740-747, September 1983.
16. Richards W. F., and Y. T. Lo, "An Improved Theory for Microstrip Antennas and Applications, "IEEE Trans, on Antennas and Propagation, Vol. AP-29, No. 1, pp. 38-46, January 1981.
17. Uzunoglu N. K., N.G. Alexopoulos and J. G. Fikioris," Radiation Properties of Microstrip Dipoles," IEEE Trans. on Antennas and Propagation, Vol. AP-27, No. 6, pp. 853- 858, November 1979.